

# The Three Hundred Project: Dynamical state of galaxy clusters and morphology from multi-wavelength synthetic maps

Federico De Luca,<sup>1,2\*</sup> Marco De Petris,<sup>2</sup> Gustavo Yepes,<sup>3</sup> Weiguang Cui,<sup>4</sup> Alexander Knebe,<sup>3,5</sup> Elena Rasia<sup>6,7</sup>

<sup>1</sup>*Dipartimento di Fisica, Università di Roma “Tor Vergata”, Via della Ricerca Scientifica, I-00133 Roma, Italy*

<sup>2</sup>*Dipartimento di Fisica, Sapienza Università di Roma, Piazzale Aldo Moro, 5-00185 Roma, Italy*

<sup>3</sup>*Departamento de Física Teórica and CIAFF, Módulo 8, Facultad de Ciencias, Universidad Autónoma de Madrid, 28049 Madrid, Spain*

<sup>4</sup>*Institute for Astronomy, University of Edinburgh, Royal Observatory, Edinburgh EH9 3HJ, United Kingdom*

<sup>5</sup>*International Centre for Radio Astronomy Research, University of Western Australia, 35 Stirling Highway, Crawley, Western Australia 6009, Australia*

<sup>6</sup>*National Institute for Astrophysics, Astronomical Observatory of Trieste (INAF-OATs), via Tiepolo 11, 34131 Trieste, Italy*

<sup>7</sup>*Institute for Fundamental Physics of the Universe (IFPU), via Beirut 2, 34014 Trieste, Italy*

Accepted XXX. Received YYY; in original form ZZZ

## ABSTRACT

We study the connection between morphology and dynamical state of simulated clusters in  $z \in [0, 1.031]$  from THE THREE HUNDRED Project cluster sample. We evaluate the dynamical state using a combination of dynamical parameters –  $\chi$  from theoretical measures and compare the results with other two relaxation criteria that come from observation measures: the morphology in mock X-ray and Sunyaev–Zel’dovich (SZ) effect images of galaxy clusters – the  $M$  indicator which is a combination of seven morphological parameters, and the offsets  $\Delta$  between the peaks or centroids of X-ray and SZ maps and the Brightest Central Galaxy (BCG) position estimated from optical maps. We study the efficiency of morphological indicators and the correlations with the dynamical state of the combined  $M$  and dynamical  $\chi$  parameters, that have the advantage of proving and collecting different aspects of the cluster structures than single parameters. An evolution with the redshift of the dynamical state is present, but the populations of the dynamical state classes differ when different radii are used. The main source of contamination in relaxed fraction inferred from morphological parameters is constituted by hybrid clusters.  $M$  combined parameter describes with the same efficiency the morphology in X-ray and SZ maps, with a correlation coefficient of  $\rho = 0.81$ . A moderately strong correlation between  $M$  and  $\chi$  is present, with a coefficient of  $\rho = -0.66$ . The offset parameters based on centroids are more sensitive to dynamical state than peaks positions offsets. The correlation with  $\chi$  for centroids is of the same order of  $M$ , with  $\rho = -(0.63-0.67)$  if SZ or X-ray centroids are respectively used.

**Key words:** galaxies:cluster:general – Galaxies: clusters: intracluster medium – methods:numerical

## 1 INTRODUCTION

Galaxy clusters represent the most massive, gravitationally bound structures in the Universe. The capability to recover a complete description of their potential well or their matter distribution is relevant for cosmological studies since their formation and growth are closely related to the underlying cosmological model (e.g. Voit 2005; Pratt et al. 2019). Most of the cluster cosmological constraints are based on the mass function, i.e., the number of clusters per mass and redshift bin. However, the cluster total mass is not directly observable but can be inferred through several complementary observational approaches. Some of these are based on certain assumptions on the clusters dynamical state. Even under this hypothesis, the measurement of the mass of clusters is not a simple task because these objects are complex systems made up of several mutually interacting components. Most of the mass in a typical cluster ( $M \sim 10^{14} - 10^{15} M_{\odot}$ ) is in the form of Dark Matter (DM) that holds together the baryonic

components: hundreds of galaxies and the hot X-ray emitting gas or Intra-Cluster Medium (ICM). For a virialized and dynamically “relaxed” cluster the assumption of the hydrostatic equilibrium to describe the gas state might be accurate. However, during merging events or when turbulent motions or compression or non-thermal heating of the ICM dominate, the equilibrium is no more in place and it is not trivial to derive the cluster mass from the radial profiles of the thermodynamical properties of the gas (density, pressure and temperature).

The impact of an ‘active’ dynamical state on the mass reconstruction can be investigated using numerical simulations. Indeed, despite a non-uniform definition of relaxed or disturbed clusters, several authors found similar deviations from hydrostatic equilibrium (Nagai et al. 2007; Rasia et al. 2012; Henson et al. 2016; Biffi et al. 2016; Pearce et al. 2020) and identify similar causes: turbulence, shock fronts, temperature inhomogeneities in the X-ray-emitting ICM, density inhomogeneities or clumps (Rasia et al. 2014; Nelson et al. 2014; Biffi et al. 2016; Planelles et al. 2017; Ansarifard et al. 2020). In this context, the masses of the disturbed clusters are underestimated up to

\* E-mail: federico.deluca@roma2.infn.it

30%, with also evidence of mass dependencies (Pearce et al. 2020; Gianfagna et al. 2020).

The cluster dynamical state is also linked to other halo properties, such as halo formation time (e.g. Mostoghiu et al. 2019; Hagggar et al. 2020) or halo concentration (e.g. Neto et al. 2007). For these reasons, its determination would be extremely useful for the cosmological use of clusters. Likely, the cluster dynamical state has direct repercussions on the cluster appearance. For this, the cluster morphology has been abundantly studied in the literature, especially in X-ray images (see e.g. Buote & Tsai 1995; Lotz et al. 2004; Rasia et al. 2013; Parekh et al. 2015; Lovisari et al. 2017; Lopes et al. 2018; Ge et al. 2018; Cialone et al. 2018).

This work continues these series of investigations by extending the analysis to an unprecedented statistics of massive clusters. We used the galaxy cluster catalogues from THE THREE HUNDRED Project<sup>1</sup>: a set of 324 cluster-centric regions of  $15 h^{-1}\text{Mpc}$  radius simulated with hydrodynamics which includes radiative physics and different sub-grid models to describe the stellar and black-holes populations. For each cluster, we produce and analyse optical, X-ray and  $\gamma$  maps, where for  $\gamma$  maps we intend the distribution of the Comptonization parameter  $y$ , related to the thermal Sunyaev-Zel'dovich effect (or tSZ, Sunyaev & Zeldovich 1972, 1980) and observed in the microwave band as a distortion of the Cosmic Microwave Background (CMB). Our specific goal is to determine how to best use the morphological information derived from these maps to efficiently describe the true dynamical state of a cluster, which in this work is parametrized by theoretical indicators computed directly from the 3D information of the simulated clusters.

This paper is structured as follows: in Sec. 2 we present some details of the simulations, the cluster catalogues, and the synthetic maps. In Sections 3 and 4 we introduce the dynamical and morphological indicators used in our analysis. Our results are discussed in Sec. 5 and our findings are summarised in Sec. 6.

## 2 DATASET

### 2.1 The Three Hundred cluster catalogue

The numerical cluster samples studied in this work belong to THE THREE HUNDRED Project, introduced in Cui et al. (2018). This consists in a series of zoomed hydrodynamic simulations of 324 cluster regions extracted from MDPL2, *The MultiDark Planck 2* simulation (Klypin et al. 2016), a  $1h^{-1}\text{Gpc}$  DM-only simulation with a cosmology consistent with Planck Collaboration et al. (2016). Considering only the most massive clusters<sup>2</sup> ( $M_{\text{vir}} \gtrsim 8 \times 10^{14} h^{-1}M_{\odot}$  at  $z = 0$ ), spherical regions were extracted from MDPL2 with radii  $R = 15h^{-1}\text{Mpc}$ , centred on the cluster highest density peaks. The Lagrangian areas of these spherical regions were computed from a low-resolution version of the MDPL2 and initial conditions were produced using the GINNUNGAGAP code (Cui et al. 2018), with multiple levels of mass refinements, keeping the original mass resolution of the MDPL2 simulation for the particles within the Lagrangian region and spawning one gas particle per DM particle. Accordingly to the Planck estimate of the cosmic baryon fraction, the gas particles in the highest-resolution volume have an initial mass

equal to  $2.36 \times 10^8 h^{-1}M_{\odot}$  while the mass of the DM particles is  $1.27 \times 10^9 h^{-1}M_{\odot}$ . In order to reduce the computational costs of the simulations, the mass resolution of dark matter outside the Lagrangian region has then been degraded in such a way to preserve the same tidal field.

Within THE THREE HUNDRED Project, the same 324 Lagrangian regions are re-simulated with different codes, however, for the specific analysis presented here, we focus only on the catalogues extracted from the GADGET-X hydrodynamical simulations. This code is a modified version of GADGET3 Tree-PM code and includes an improved SPH scheme with Wendland interpolating C4 kernel, artificial thermal diffusion and time dependent viscosity. Other main features of these runs are gas cooling with metal contributions, star formation with chemical enrichment and feedback from stars in the asymptotic giant branch, supernovae, and active galactic nuclei. For a more detailed description of THE THREE HUNDRED Project, see the works of Cui et al. (2018); Wang et al. (2018); Mostoghiu et al. (2019); Arthur et al. (2019); Ansarifard et al. (2020); Hagggar et al. (2020); Kuchner et al. (2020); Li et al. (2020); Knebe et al. (2020).

During the simulation production phase, we store the data for 128 different snapshots in the redshift range between  $z = 17$  and  $z = 0$ . In this work we analyse clusters coming from 10 selected redshifts: 0, 0.116, 0.193, 0.304, 0.457, 0.557, 0.663, 0.817, 0.900 and 1.031. This choice has been made to study the redshift evolution of both the morphological parameters and the dynamical state indicators. The partial redshift overlap with Cialone et al. (2018, hereafter C18) allows to compare the results with those from the MUSIC simulation.

### 2.2 Mock optical, X-ray and SZ maps

We generate three maps per cluster reproducing optical, X-ray and millimetre observations. The last category is aimed to mimic maps from the tSZ effect. They are produced considering a spherical region of radius  $1.4R_{200}$ , centred on the projected position of the theoretical cluster centre defined here as the maximum of the density. Only the projection along the  $z$ -direction is used in this paper. However, we note here that the other projections give similar results. All synthetic maps are produced without including the contribution of other sky contaminants or instrumental noise. Finally, the resolution of each map is specified below.

The **optical maps** of the clusters reproduce the optical  $r$  band of the Sloan Digital Sky Survey (SDSS), with the same angular resolution of  $0.396''$  per pixel. The main sources in this band are galaxies whose stellar luminosities are derived applying a stellar population synthesis code described in Cui et al. (2011, 2014, 2016). This code provides the galaxy spectral energy distribution from far-UV to radio, for an instantaneous starburst of a given mass, age and metallicity. The total flux from stars is then calculated assuming a Chabrier initial mass function (Chabrier 2003), which is also adopted in GADGET-X. The maps are produced in unit of:  $[\text{erg s}^{-1} \text{cm}^{-2}]$ .

Galaxy clusters are strong and extended sources in the **X-ray band**. The X-ray emission is due to the process of thermal bremsstrahlung in which hot electrons are scattered by ions in the ICM. The surface brightness  $\Sigma_X$  along the line of sight can be written as:

$$\Sigma_X(\nu) = \frac{1}{4\pi(1+z)^3} \int n_e n_i \Lambda_X(T, Z, \nu) dl, \quad (1)$$

where  $n_e$ ,  $n_i$  are the electrons and ions number densities and  $\Lambda_X(T, Z, \nu)$  is the cooling function which depends on the frequency  $\nu$ , the metal abundances  $Z$  and the temperature of the plasma  $T$ . X-ray images are produced using PYXSIM CODE (ZuHone et al. 2014). The

<sup>1</sup> <https://the300-project.org>

<sup>2</sup> In this paper, we indicate with  $R_{\Delta}$  the radius of the sphere whose density is  $\Delta$  times the critical density of the Universe at that redshift  $\rho(R_{\Delta}) = \Delta \rho_{cr}(z)$ . We specifically use overdensities equal to  $\Delta = 500, 200$ , and  $\text{vir}$ , where  $\Delta_{\text{vir}}$  corresponds roughly to 98 for the assumed cosmological model.

X-ray maps are in terms of number counts of detected photons and their spectral band is 0.1-15 keV. We use the responses associated to the WFI instrument which will be on-board of the Athena satellite (Rau et al. 2013).

The **SZ effect** is originated through inverse Compton scattering of CMB photons with ICM hot electrons. The distortion is caused both by the random thermal motion of electrons and by the overall bulk motion of the cluster with respect to the Hubble flow (kinematic SZ effect). Clusters maps in microwave band are dominated by the thermal SZ, since for the expected velocities of galaxy clusters (few hundred km s<sup>-1</sup>), and typical cluster temperatures (few keV) the kinematic contribution is about 10 per cent of the thermal one (Birkinshaw 1999; Carlstrom et al. 2002). Therefore in our analysis, we studied only the thermal SZ maps that could be described in terms of the 2D distribution of the dimensionless Comptonization parameter  $y$ . It is defined as:

$$y = \int n_e \sigma_T \frac{kT_e}{m_e c^2} dl, \quad (2)$$

where  $m_e$  and  $T_e$  are the electron mass and temperature,  $\sigma_T$  is the Thomson cross section,  $c$  the speed of light,  $k$  the Boltzmann constant and  $dl$  is the line of sight length. Operationally, we compute a discretised version of Eq. (2) for which we assume that  $dV = dAdl$  and  $dA$  is the pixel area (Sembolini et al. 2012; Cui et al. 2018):

$$y = \frac{\sigma_T k}{m_e c^2 dA} \sum_i T_i N_{e,i} W(r, h_i), \quad (3)$$

where  $N_{e,i}$  is the number of electrons,  $h_i$  the SPH smoothing length and  $W(r, h_i)$  the SPH smoothing kernel used in the simulation. The  $y$  maps are produced by the `pyMSZ` code<sup>3</sup>, which can also generate the kinematic SZ effect maps simultaneously (see Baldi et al. 2018, for MUSIC simulation).

Both ICM maps have a fixed spatial comoving resolution of 10 kpc pixel<sup>-1</sup>. Notice that the X-ray and  $y$  maps give complementary information about the cluster structure. SZ effect data are more effective in describing the cluster outskirts compared to X-ray images since the  $y$  signal is roughly linearly dependent on the electron density while the X-ray emission is instead proportional to density square.

The following analysis based on the maps considers the map centroids as reference centre instead than the theoretical cluster centre to not bias our results by a priori knowledge of the true cluster centre. The centroids of the X-ray and  $y$  maps are calculated considering the emission of all pixels within a circle of radius equal to  $R_{500}$ .

All maps are used to extract the morphological parameters described in Sec. 4.1, while in the next Section we introduce the indicators of the dynamical state computed using the 3D information.

### 3 DYNAMICAL STATE INDICATORS

In the case of hydrodynamical simulations, all the physical properties of each particle are known. Therefore for a given object, it is possible to estimate all the physical quantities in interest, such as density, gravitational potential, pressure, mass, etc. The theoretical indicators of the dynamical state applied to simulations use this advantage and thus refer to quantities computed in 3D that would be unreachable from an observational analysis.

Throughout the paper, we use five indicators either to compare to

the MUSIC simulations in C18 and THE THREE HUNDRED clusters in Cui et al. (2018) or to compare with the morphological parameters: (i) the mass fraction of all sub-halo over the cluster,  $f_s$ , (ii) the ratio between the masses of the most massive substructure and the cluster,  $f_{s,mm}$ , (iii) the offset between the cluster centre and the centre of mass,  $\Delta_r$ , (iv) the ratio between thermal and potential energy,  $\eta$ , and (v) the relaxation parameter  $\chi$  (Haggar et al. 2020). In the following we will describe each of them with more details, but not before underlining that in literature there are many applications of these parameters for the relaxation definition (see Neto et al. 2007; Macciò et al. 2007, 2008; Duffy et al. 2008; Klypin et al. 2011; Klypin et al. 2016; Cui et al. 2017; Barnes et al. 2017; Pearce et al. 2020).

Identifying all the sub-halos present inside a spherical region of a cluster with radius  $R_{ap}$ , the total sub-halo mass fraction  $f_s$  is defined as the ratio between the sum of all the sub-halo masses respect to the cluster mass within such volume,  $M_{ap}$ :

$$f_s = \frac{\sum_i M_i}{M_{ap}}. \quad (4)$$

Halos and sub-halos are identified with the Amiga Halo Finder, AHF<sup>4</sup> (Knollmann & Knebe 2009), whenever the structure has at least 20 particles.

The other mass fraction indicator is built considering only the contribution of most massive substructure in the cluster:

$$f_{s,mm} = M_{mm}/M_{ap}. \quad (5)$$

The virial ratio  $\eta$  is based on the virial theorem and it is defined as:

$$\eta = \frac{2T - E_s}{|W|}, \quad (6)$$

where  $T$  is the total kinetic energy,  $E_s$  is the surface pressure energy from both collisionless and gas particles, and  $W$  is the total potential energy (see Cui et al. 2017, for details).

The offset of the centre of mass  $\Delta_r$  is quantified as:

$$\Delta_r = \frac{|\mathbf{r}_{cm} - \mathbf{r}_c|}{R_{ap}}, \quad (7)$$

where  $\mathbf{r}_{cm}$  is the position of the centre of mass of the cluster and  $\mathbf{r}_c$  is the theoretical centre of the cluster which we recall we identify as the position of the highest density peak.

Finally, in order to describe the degree of relaxation Haggar et al. (2020) proposed to use the inverse square root of the normalised quadratic mean of various indicators, generically indicated as  $x_i$ :

$$\chi = \left[ \frac{\sum_i \left( \frac{x_i}{x_{0,i}} \right)^2}{N} \right]^{-1/2}, \quad (8)$$

where  $x_{0,i}$  are the classification thresholds used to distinguish between relaxed and disturbed clusters. Unfortunately, in literature, there is not a unique selection of these thresholds and also of the set of 3D dynamical indicators ( $x_i$ ) that are the most suitable to segregate among relaxed and disturbed clusters (see also Cui et al. 2017). The variety of choices made by different authors is partially justified from the fact that different kinds of simulations were involved (e.g. DM versus hydrodynamical runs with different treatments for the baryon physics) or because the dynamical state indicators were extracted from different volumes such as those within  $R_{vir}$  or  $R_{200}$  or  $R_{500}$ . In fact, by including the most external regions, volumes that are less

<sup>3</sup> <https://github.com/weiguangcui/pymsz>

<sup>4</sup> <http://popia.ft.uam.es/AHF>

virialized become part of the analysis and these are characterised by more substructures that are still in the process of merging into the cluster. Studying these dependencies is one of the goals of this paper.

In addition to the usage of a continuous parameter, such as the combined  $\chi$  parameter defined above, we also classify the clusters in three separate classes called ‘relaxed’, ‘hybrid’, and ‘disturbed’. These classes are defined by using the parameters  $f_s$  (Eq. 4) and  $\Delta_r$  (Eq. 7). Specifically, we defined relaxed (disturbed) all objects for which the two conditions  $f_s < 0.1$  and  $\Delta_r < 0.1$  ( $f_s > 0.1$  and  $\Delta_r > 0.1$ ) are simultaneously verified. The hybrid class includes all other clusters, i.e., those for which the two inequalities have different signs. This class-based division will be useful to compare with other works present in literature.

In this work, we studied the dynamical state of THREE HUNDRED clusters in Sec. 5.1 and we specifically compare the results of different relaxation criteria on THREE HUNDRED sample in Sec. 5.2. We select and tune the best morphological parameters among those that better segregate relaxed from disturbed clusters by using as prior our knowledge on the systems’ dynamical state as measured from the 3D dynamical indicators. The procedure will be described in Sec. 4 and applied in Sec. 5.3.

#### 4 MORPHOLOGICAL INDICATORS

Historically, the morphology of clusters has been studied using several parameters applied to the different multi-wavelength maps (e. g. Okabe et al. 2010; Meneghetti et al. 2014; Lovisari et al. 2017; Bartalucci et al. 2019; Cao et al. 2020, with references therein). Most of the ICM morphological indicators have been originally introduced for X-ray cluster maps (Santos et al. 2008; Nurgaliev et al. 2013; Mantz et al. 2015) to detect the presence of substructures (Mohr et al. 1993; Buote & Tsai 1995; Poole et al. 2006; Jeltema et al. 2008) and were borrowed and adapted from optical studies on the galaxy morphology (Rasia et al. 2013), or even from optics analysis as the application of Zernike polynomials to cluster maps (Capalbo et al. 2020). The cluster dynamical state can also be inferred from some optical substructure estimators, based on galaxies properties such as local deviations from global mean and dispersion of radial velocities, magnitude difference between the Brightest Central Galaxy (BCG) and the second brightest galaxy (e.g. Pinkney et al. 1996; Lavoie et al. 2016; Lopes et al. 2018, and reference therein), and offsets between the BCG and the X-ray peak or X-ray centroid (Sanderson et al. 2009; Mann & Ebeling 2012; Mahdavi et al. 2013; Rossetti et al. 2016; Lopes et al. 2018; Zenteno et al. 2020).

In this paper, we applied seven ICM morphological indicators on our X-ray and y maps, plus a combination of them. The combination of various parameters into one is a strategy already used in literature (Rasia et al. 2013) since each parameter highlights only a particular aspect of a typical disturbed system and, at times, the efficacy of one parameter in describing the cluster dynamical status depends on the chosen line of sight as projections might influence the result (C18). Together with this set of parameters based on the ICM appearance, we have also studied parameters based on the offsets between BCG and X-ray and y peaks or centroids positions.

The definitions of all these parameters are described in Sections 4.1 and 4.2, while in Sec. 4.3 the diagnostic ability of morphological parameters is studied by using the Kolmogorov-Smirnov (KS) two tail test, and the analysis of the Receiver Operating Characteristic (ROC) curve (see e.g. Swets 1988; Fawcett 2006, for a more detailed introduction of ROC diagnostic test). Finally, the segregation ability

of the morphological parameters is tested comparing them with the 3D dynamical indicator  $\chi$  in Sec. 5.

##### 4.1 ICM morphological indicators

The morphological indicators for X-ray and y maps used in this work are the same described in C18 for MUSIC simulation:

*A*, Asymmetry (Schade et al. 1995; Okabe et al. 2010; Zhang et al. 2010) is a normalised difference between the original map and a rotated one. For our analysis, we analyse 4 different rotations of the maps (90°, 180° and the flipped images along the main axes) and then we consider, for each cluster, the rotation which maximises *A*;

*c*, Light Concentration Ratio (Santos et al. 2008) is the ratio of the surface brightness, computed inside two concentric apertures;

*w*, Centroid Shift (Mohr et al. 1993; Poole et al. 2006; O’Hara et al. 2006; Böhringer et al. 2010) is the average of the shifts of the centroids obtained from various concentric circles with increasing radius;

*P*, Power Ratio (Buote & Tsai 1995) is based on a multipole decomposition applied to the maps of the ICM which are thought to represent the projected mass distribution;

*G*, Gaussian Fit (C18) is the ratio of the two standard deviations of a 2D Gaussian fit to the X-ray and y maps;

*S*, Strip (C18) is defined as a normalized difference of *N* light profiles, passing through the centroid. Following C18, we compare 4 strips inclined by 45° respect to each other.

As for the 3D dynamical indicators, the morphological indicators depend on the aperture,  $R_{ap}$ , used to estimate them. To determine which aperture is the most efficient in separating the clusters, we employ the same procedure illustrated in C18. For each aperture, we create two distributions of the morphological parameters relative to the clusters of both the relaxed and disturbed classes introduced at the end of the last session. With these two distributions as input, we compute the KS test and consider the best aperture as that corresponds to the minimum of the median of all KS-p values, over the entire redshift range. The results of this tuning are shown in Sec. 5.3. All these tuned parameters  $V_i$  are then collected in the combined parameter *M*, defined as in C18:

$$M = \frac{1}{\sum_i W_i} \left( \sum_i W_i \frac{\log_{10}(V_i^{\alpha_i}) - \langle \log_{10}(V_i^{\alpha_i}) \rangle}{\sigma_{\log_{10}(V_i^{\alpha_i})}} \right), \quad (9)$$

where  $\alpha_i = \pm 1$ , depending on how the *i*-th parameter is related to the dynamical state. *M* parameter represents a weighted average of the standardised indicators described above, to enhance and have a single parameter to characterise the morphology. The logarithm of the minimum KS-p median value over the entire redshift range is used as a weight,  $W_i$ , in *M* definition (Eq.(9)), for each parameter:

$$W_i = \left| \log_{10} \left( \min \left\{ \widetilde{KS}\text{-}p_{i,z} \right\}_{R_{ap}} \right) \right|. \quad (10)$$

##### 4.2 Offset morphological indicators

On top of the ICM-based morphological indicators, we used also the offset between the BCG position and both the centroids and the peaks of the X-ray and y maps (Lavoie et al. 2016; Lopes et al. 2018). As an example, we visualise all relevant positions in Fig. 1. In general, the BCG position is expected to trace the position of the matter density peak inside clusters (Cui et al. 2016), as postulated in the “Central Galaxy Paradigm” (Tremaine 1990; Postman & Lauer 1995; Lin & Mohr 2004; Lopes et al. 2018). We studied the validity of the Central



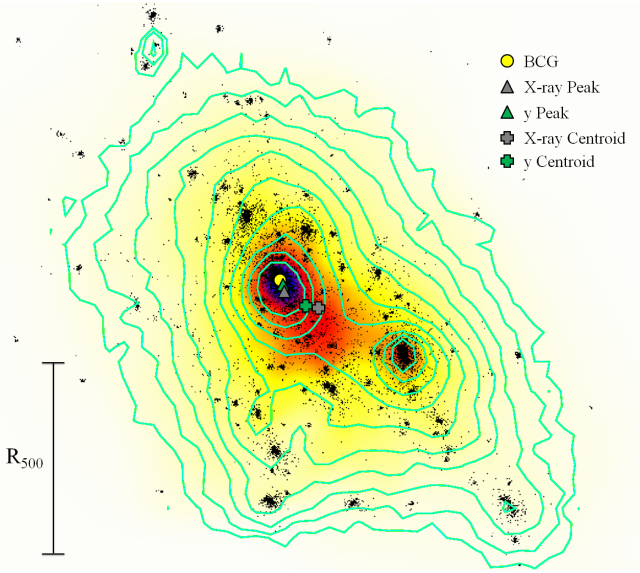


**Figure 1.** Multi-wavelength map of the cluster at  $z = 0.46$ , in region 85 of the simulation. The  $y$  colourmap and X-ray photon counts contours in log scale are superimposed to the optical SDSS  $r$  band. Isocontour levels are logarithmic equispaced by a factor  $\log 2$ . The position of the BCG (yellow dot), X-ray and  $y$  peaks (grey and green triangles) or centroids (crosses) are also drawn in the figure.

Galaxy Paradigm and the efficiency of these offset parameters in Sec. 5.4.

### 4.3 Methods to estimate the efficiency of the morphological parameters

In this work, we studied the performance of our morphological classifiers using two different tests: the Kolmogorov-Smirnov test and the analysis of ROC curves to which we associate and study several diagnostic parameters. The KS test is a statistical non parametric test that determines whether two samples are representative of the same distribution by comparing their cumulative distribution function. This test returns the maximum deviation between the two curves and a parameter referred to as  $p$  value which provides the significant level of the result. A small  $p$  value implies that the two distributions are different.

As explained in Sec. 4.1, the KS test is used to retrieve the best aperture to calculate the six morphological parameters. In particular, using the dynamical state classification as a prior, we can compare the relaxed and disturbed distributions of the morphological parameters estimated in different aperture with the KS test. This process is repeated for all redshifts. Then for each morphological parameter, we consider the median of the KS- $p$  values as reference to determine the best overall aperture. These medians are used also to compute the combined parameters as in Eq. 10.

Generally, for the classification of clusters in observations, we applied continuous morphological parameters  $V$  to divide them in categories. To do that, we select a threshold  $V_T$  on those parameters above (below) which the clusters are morphological regular (disturbed). This classification will reflect the dynamical state according to the efficiency of the parameter, that can be described in terms of false and true detection. If a cluster is dynamical relaxed but does not satisfy the morphological threshold, we can define this

case as a false negative ( $FN$ ), wrong classification. Classifying instead a disturbed cluster as regular we will have a false positive ( $FP$ ) case. Viceversa, the proper selections are defined as true positive ( $TP$ , the morphologically and dynamically relaxed) or true negative ( $TN$ , the morphologically and dynamically disturbed) objects. All these outcomes are generally collected together in the contingency (or confusion) matrix. Several evaluation metrics can be defined from these four classes, as the completeness ( $C$ ), the purity ( $p$ ) (Rasia et al. 2013), or the Matthews correlation coefficient ( $MCC$ ). The selection of the threshold  $V_T$  is crucial for the classification, since changing this value we will modify the result of the classification and the diagnostic power of the used classifier. To characterise that dependence for our morphological parameters, we study the ROC curves associated to the dynamical state described by the three classes defined in Sec. 4.

**Completeness.** The completeness quantifies how many correct identifications are performed in the test and it is defined as the true positive rate,  $TPR$ , the number of correct classifications divided by the total number of relaxed clusters:

$$C = TPR = \frac{TP}{TP + FN}. \quad (11)$$

**Purity** The purity instead describe the presence of contaminants in the selected sub-sample of only regular clusters, and it is defined as:

$$p = \frac{TP}{TP + FP}. \quad (12)$$

**Matthews correlation.** The  $MCC$ , equivalent to Pearson  $\phi$  coefficient, is instead defined considering all the terms of the confusion matrix, taking care of unbalanced samples distribution:

$$MCC = \frac{TP \times TN - FP \times FN}{\sqrt{(TP + FP)(TP + FN)(TN + FP)(TN + FN)}}. \quad (13)$$

**ROC curves.** Letting the threshold  $V_T$  vary, the ROC curve is defined as the graph of  $TPR$  (the completeness  $C$ ) against the false positive rate  $FPR$ , the number of disturbed clusters incorrectly recognised as relaxed, in terms of the total number of disturbed objects:

$$FPR = \frac{FP}{TN + FP}. \quad (14)$$

The ROC curve is a powerful graphical test: in the case of a perfect classifier, the associated ROC curve will be described in  $TPR$ - $FPR$  plane by a unit step function. On the contrary, an indicator that has equal probability to recognise a cluster as relaxed or disturbed is instead described in the same plane by the identity line. From the properties of this curve, several summary statistics for the diagnostic power are commonly drawn, such as the area under the curve ( $AUC$ ), with  $AUC = 0.5$  associated with random guess and  $AUC = 1$  to the perfect case, or the Youden's  $J$  statistics. The Youden's  $J$  statistics is defined as:

$$J = TPR + TNR - 1, \quad (15)$$

where  $TNR$  is the true negative rate (the number of clusters that are correctly recognised as non-relaxed over the total number of non-relaxed clusters). It represents, graphically, the ROC height above the random guess line.

**Probability.** Another simple way to estimate the diagnostic ability of the parameters and the contamination of non-relaxed classes is to

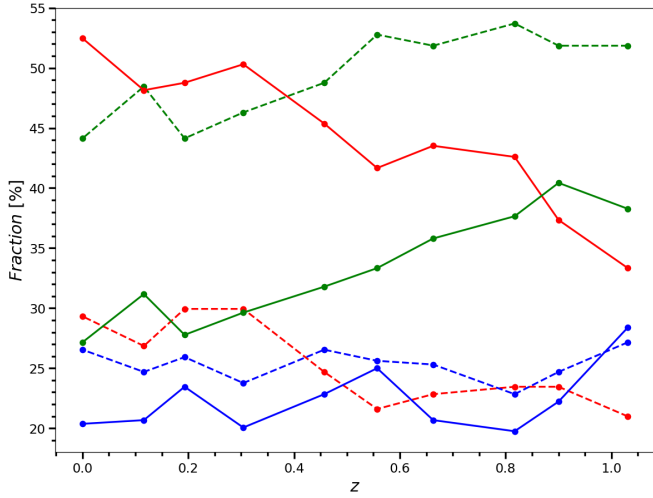


**Figure 2.** Percentage of relaxed (red lines), hybrid (green), disturbed (blue) clusters along the redshift, using as volume radius  $R_{200}$  (dashed line) and  $R_{500}$  (solid line).

define a probability,  $P$ , to count in our sample a relaxed, hybrid or disturbed cluster for a given value of the classifier  $V$ . A simple merit function to quantify this can be defined as:

$$P_z^{r,h,d}(V) = \frac{N_z^{r,h,d}(V)}{N_z^r(V) + N_z^h(V) + N_z^d(V)}, \quad (16)$$

where  $N_z^{r,h,d}$  is the number of relaxed (subscript r), hybrid (h) or disturbed (d), objects that have a certain value  $V$  for redshift  $z$ . The purity  $p$  corresponds to the integral of  $P$ :  $p = \int P dV$ .

In this work, we use ROC curve,  $AUC$ ,  $J$ ,  $MCC$ ,  $C$ ,  $p$  and  $P$  to study the efficiency and the purity of sub-samples when a threshold is applied to morphological parameters. In particular, we use  $MCC$  and  $J$  to infer a suitable and not arbitrary threshold ( $V_T$ ) on morphological parameters to divide relaxed objects from the other cases. In fact,  $J$  and  $MCC$  can be used as a score for the performance of the test: their (absolute) value ranges from 1 through 0, depending on whether the test is able or not to discriminate between the two classes. Considering that the performance of the test changes if the discrimination threshold is varied, we can choose as threshold the one that maximises these two evaluation metrics. A detailed discussion of the consistency of relaxed sub-samples inferred with different criteria is beyond the goal of this paper. However, we still compare the fraction of relaxed clusters available in literature (see also [Rasia et al. 2013](#); [Mantz et al. 2015](#); [Rossetti et al. 2016](#); [Lovisari et al. 2017](#); [Cao et al. 2020](#), and references therein) with our findings in Sec. 5.5.

## 5 RESULTS

In this Section, we discuss the dynamical state of clusters and the segregation efficiency of the morphological parameters described in Sections 4.1 and 4.2. Then in Sec. 5.5, we compare our morphological results with other clusters samples, available in literature.

### 5.1 Dynamical state of Three Hundred Galaxy Clusters

In Fig. 2 we show the percentage of relaxed, hybrid and disturbed classes as a function of redshift. Dashed and solid lines refer to

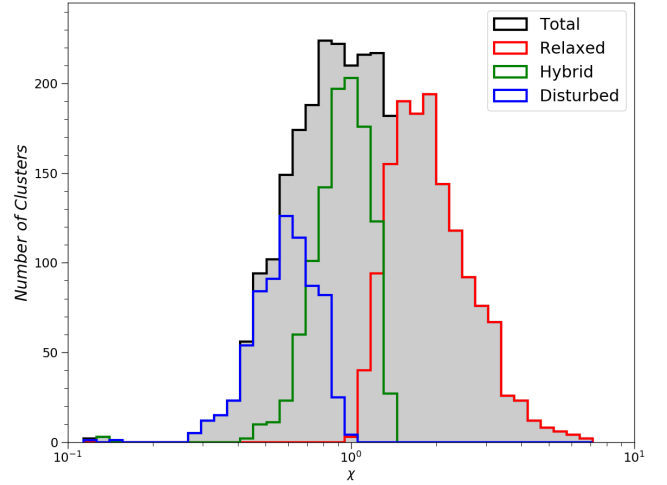


**Figure 3.** Distribution of  $\chi$  from dynamical indicators inside  $R_{500}$ , for all the redshift. Blue, green and red curves correspond to the disturbed, hybrid and relaxed classes distributions.

measurements done within  $R_{200}$  and  $R_{500}$ , respectively. The relaxed and hybrid populations show a redshift evolution with reverse trends: the relaxed fraction decreases while the hybrid fraction increases from  $z = 0$  to  $z = 1$ . At the same time, the disturbed class remains almost constant. This redshift evolution is expected since clusters start to relax at about  $z \sim 1$  but the majority reaches a virialization status only by  $z=0$  ([Muldrew et al. 2015](#)). The hierarchical cluster evolution can also explain the quite different percentage of objects defined as relaxed within  $R_{500}$  (above 50 per cent at  $z = 0$ ) and within  $R_{200}$  (30 per cent at  $z = 0$ ). The strong decrease associated to the largest volume suggests that several substructures are present in the cluster outskirts and they have not reached a relaxation status yet. Although, since the disturbed class does not dramatically change, the cluster outskirts affect only one of the two parameters entering into the relaxation definition (either  $f_s$  or  $\Delta_r$ ). As already noted we recall that the exact value of the relaxed cluster fraction depends not only on the volume considered but also on the chosen threshold ( $x_0$ ) as we will explore in the next Section and in Fig. 4.

For the study of the connection between the dynamical state and morphology of clusters, we decide to limit our analysis only to regions inside  $R_{500}$ . This choice was done in order to study the same region commonly achievable in observations and therefore we will consider the dynamical state defined inside that aperture, as for Fig. 3 where we show the distribution of the continuous  $\chi$  obtained from these same parameters ( $x_i = (f_s, \Delta_r)$ ) and thresholds ( $x_{0,i} = 0.1$  for both) that we use for the dynamical classification scheme. The distribution is drawn including all clusters at all redshifts. Over-plotted we also show the distributions of the relaxed, hybrid, and disturbed classes (see Sec. 3) in red, green, blue colour, respectively. By definition, relaxed (disturbed) systems have  $\chi$  greater (lower) than 1. The hybrid systems, instead, occupy the region between the two extreme population.

### 5.2 Impact of different criteria on dynamical state

In this Section, we want to compare our findings with previous results appeared in the literature. For this, we adopt the same criteria used in [C18](#) and [Cui et al. \(2018\)](#) and, as before, we compute the indicators within both  $R_{500}$  and  $R_{200}$ . In [C18](#) the dynamical state

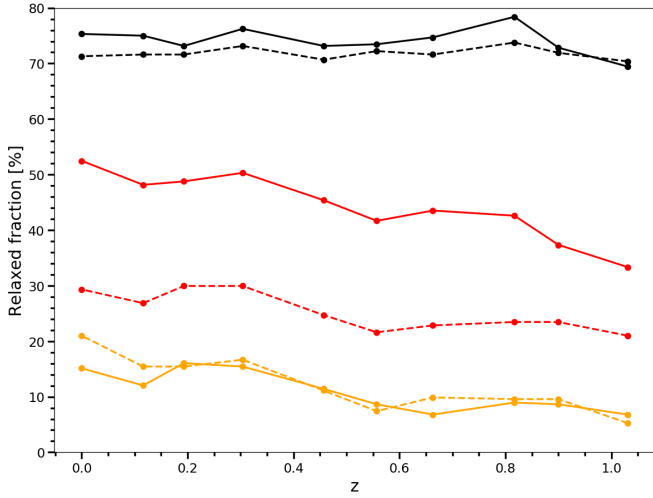


**Figure 4.** Percentage of relaxed clusters at different redshift, applying the relaxation criteria defined in this work (red), in Cui et al. (2018) (orange) and C18 (black) using  $R_{200}$  (dashed lines) and  $R_{500}$  (solid lines).

of the MUSIC galaxy clusters is studied within  $R_{vir}$ , using  $\Delta_r$  and  $f_{s,mm}$ . Relaxed clusters are those who have at the same time  $\Delta_r$  and  $f_{s,mm}$  less than 0.1. Instead in Cui et al. (2018) THE THREE HUNDRED relaxed clusters are defined by adopting more stringent criteria since all the following conditions, measured within  $R_{200}$ , needed to be simultaneously satisfied:  $|1 - \eta| < 0.15$ ,  $\Delta_r < 0.04$  and  $f_s < 0.1$ .

The relaxed fractions of THE THREE HUNDRED clusters adopting these criteria, calculated for  $R_{200}$  (solid lines) and  $R_{500}$  (dashed lines) are shown in Fig. 4. When we apply to our samples the C18 criteria we recover one of the results highlighted in that paper: the relaxed fraction is constant in the redshift range considered, that, here ( $0 < z = 1$ ) is more extended than in C18 ( $0.4 < z < 0.8$ ). We notice that the relaxed fraction remains almost constant both considering  $R_{500}$  or  $R_{200}$ . It is, however, striking the difference in the amount of relaxed clusters: up to 70% here (black lines) and close to 50% in C18 paper. This discrepancy is again explained by the fact that in C18 all quantities were defined within  $R_{vir}$  and therefore contained the less virialized external regions. To be sure that this interpretation is correct we analysed only for sake of this comparison also THE THREE HUNDRED runs carried out with the code GADGET-MUSIC. We consider only  $z = 0$  clusters and evaluate all parameters within  $R_{vir}$ . In this case, it is recovered the same fraction of MUSIC relaxed clusters. The absence of a dynamical evolution is mainly due to the fraction in mass indicator ( $f_{s,mm}$ ) used in C18 paper. This parameter significantly changes only when a great substructure enters into the dominant halo and does not consider all the other substructures as  $f_s$  does (Fig. 2). Therefore, for this work we prefer to consider  $f_s$  because more sensible to even minor mergers which are expected to perturb the ICM at the same level.

As shown in Fig. 4, the criteria of Cui et al. (2018) return, instead, a much smaller percentage of ‘relaxed’ objects for two main reasons: they consider as a factor also the energy virial ratio and they impose a stronger condition on  $\Delta_r$  (0.04 versus 0.1). As a result, less than 20% of the clusters are now recognised as relaxed, with a redshift dependence similar to the one found here (Fig. 2). Interestingly, using these criteria the results related to  $R_{200}$  and  $R_{500}$  are almost the same. We verified that the absence of an aperture dependency is due to the introduction of  $\eta$ : this parameter has an opposite dependency on the explored volume respect to the others. When we consider exclusively

**Table 1.** Radii of the best apertures in units of  $R_{500}$  and relative weights ( $W_i / \sum_i W_i$ ) of all the parameters. In the case of  $c$  parameter the two radii of the concentric apertures are listed.

| morphological<br>parameters | X maps        |         | y maps |              |         |      |
|-----------------------------|---------------|---------|--------|--------------|---------|------|
|                             | $R_{ap}$      | KS-p    | $W$    | $R_{ap}$     | KS-p    | $W$  |
| $A$                         | 0.50          | 8.6e-15 | 0.17   | 1.00         | 1.2e-11 | 0.16 |
| $c$                         | 0.025<br>0.25 | 3.4e-20 | 0.24   | 0.05<br>0.25 | 6.6e-21 | 0.29 |
| $P$                         | 0.25          | 5.3e-17 | 0.20   | 0.50         | 1.2e-9  | 0.13 |
| $w$                         | 1.00          | 6.3e-16 | 0.19   | 0.75         | 1.9e-17 | 0.24 |
| $G$                         | 0.50          | 4.7e-5  | 0.05   | 0.25         | 9.3e-4  | 0.04 |
| $S$                         | 1.00          | 4.1e-13 | 0.15   | 1.00         | 5.7e-10 | 0.13 |

the  $\eta$  parameter, we have more relaxed clusters at  $R_{200}$  (63% at  $z = 0$ ) than at  $R_{500}$  (close to 34%). This is due to the definition of  $\eta$ : it was initially introduced to study the dynamical state of isolated objects. Therefore, estimating it inside the clusters leads to other contribution in  $E_s$  due to the interaction between the external regions of the clusters and the inner ones. Therefore this criterion could be used to restrict the analysis only to the ‘very relaxed’ cluster subsample considering  $R_{200}$ , for which the hydrostatic assumption is more fulfilled.

### 5.3 X-ray and y maps morphology

With the procedure described in Sections 4.1 and 4.3, we use the dynamical state classification results in the KS test to estimate the best aperture and the weights (Eq. 10) of the morphological parameters for X-ray and y maps. For the KS test, we calculate the parameters inside 4 equally spaced fractions of  $R_{500}$ , and in case of the  $c$  parameter we consider 10 equally spaced inner radii varying in the range  $[0.1 - 1]R_{ap}$ .

The tuning procedure of X-ray and y maps morphological indicators with the KS test returns small probability  $p$ -values, but their variance changes of several orders of magnitudes over redshift. For example, we have  $p \sim 10^{-7}$  ( $z = 0$ ) and  $p \sim 10^{-3}$  ( $z = 1$ ) for y maps  $P$  parameter, with an aperture of  $R_{500}$ . Although a decrease of performances is expected for most of the parameters for higher redshifts, we decided to use the median of KS-p value in C18 tuning procedure, instead of average, to be less affected by outlier and to obtain a single best aperture suitable for all the redshifts. In Table 1 the best apertures from the KS-test tuning procedure and weights for  $M$  parameter are listed. The weights are expressed as fractions of  $W_T = \sum_i W_i$ , with  $W_T = 82$  for X-ray and  $W_T = 69$  for y maps, to clearly show which parameter contributes more in  $M$ .

Although most of the parameters are originally defined for X-ray observations, they show similar results also on y maps. Two examples are the parameters  $c$  and  $w$  that weights even more in y maps than in X-ray maps for which they were introduced at first. The results of the KS analysis in the two sets of maps mostly differ for the identification of the best aperture to be used to compute the morphological indicators. The indicators that are influenced by small-scale variations favour a small aperture in the X-ray maps where the substructures are more evident. Indeed, some small central clumps might be in pressure equilibrium and therefore are hidden in the y maps. Viceversa, the parameters that mostly consider large-scale inhomogeneity are better traced with a larger aperture in X-ray in order to capture more of the

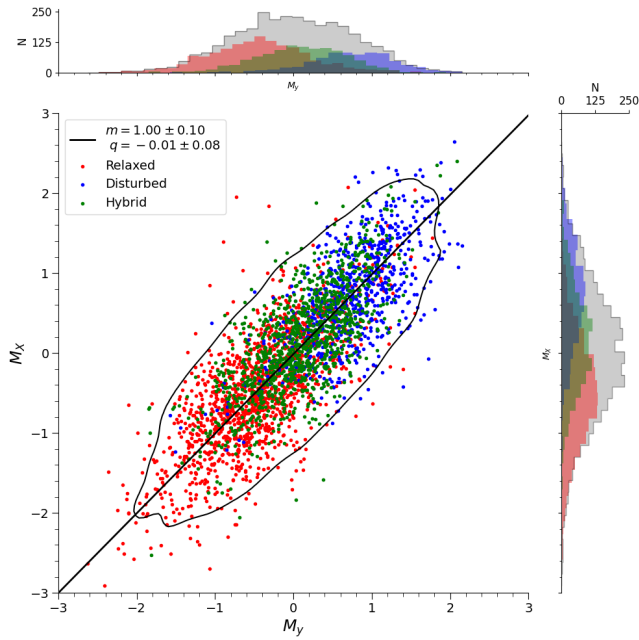


**Figure 5.** Scatter plot of relaxed (red), hybrid (green) and disturbed (blue) clusters  $M$  values and their distributions for the complete redshift sample. The linear fit is also plotted in the figure, with the 95% confidence level of the data distribution.

external signal, which is weaker with respect to the  $y$  maps. Looking at the weights that each parameter carries, we notice that the  $G$  parameter, as highlighted also by C18, is the least effective parameter and it contributes to the combined parameter  $M$  only three or four time less.  $G$  gives a global estimation of how much a cluster is prolate or oblate and does not take into account the detailed internal structure of ICM. Moreover, the spherical shape assumption even for a relaxed cluster is a rare case: most clusters are better described by an ellipsoidal shape and the  $G$  parameter, thus, become less robust because it can strongly vary depending on the chosen projection.

A linear correlation between  $M_y$  and  $M_x$  is present, as shown in Fig. 5, with a Spearman correlation coefficient of  $\rho = 0.81$ . From this figure and hereafter, all the fits are performed with a least-square algorithm to reduce the effect of outliers or leverage points present in the data. For the  $M_y$ - $M_x$  relation, the best fit is in agreement with the line of equality, indicating that, on average, this set of indicators works efficiently both on X-ray or  $y$  maps. From the marginal distributions in the top and side panels of Fig. 5, the most common clusters in our sample are morphological hybrid clusters, since the peaks of the  $M$  distributions are close to  $M \sim 0$ , while the two tails are associated with the more relaxed (negative tail) and more disturbed (positive) clusters. It is relevant to stress how both these distribution are remarkably similar to the  $\chi$  distribution already shown in Fig. 2. The relation between the dynamical and morphological state is shown in Fig. 6, where the scatter plot between the two parameters,  $\chi$  and  $M$ , is studied. The Spearman coefficient indicates a relatively strong correlation:  $\rho \sim -0.66$ , using  $M$  from either  $y$  or X-ray maps. As a result, the  $M$  parameter derived from these maps could be used as a single good proxy of the dynamical state of galaxy clusters, since it represents a dynamical state weighted combination of different morphological aspects of clusters. In Fig. 5 and Fig. 6 we have also distinguished with colours the three classes that we defined in Sect. 3: relaxed, hybrid, disturbed. Our intent is to show

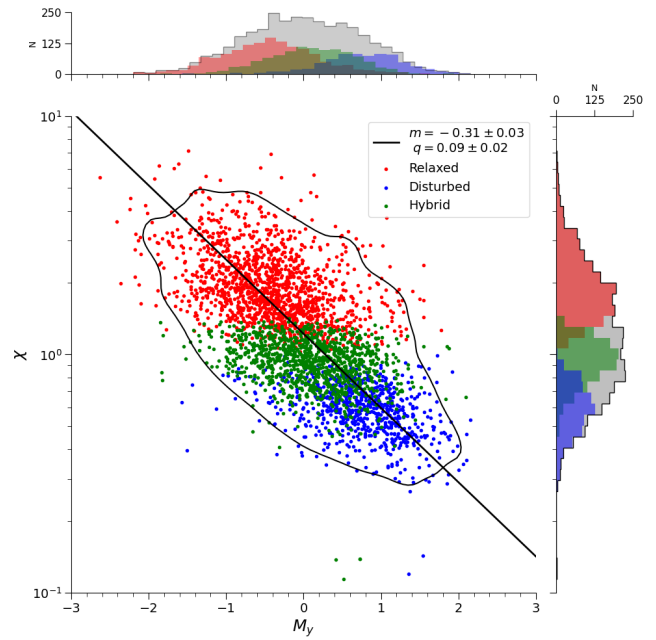


**Figure 6.** Scatter plot in semilog scale between  $\chi$  and  $M_y$ , with their distributions in the marginal plots. Straight line corresponds to a linear fit of the data and red, green, blue colours are associated to the relaxed, hybrid and disturbed dynamical classes. The 95% confidence level of the data is also shown in the figure.

how a rigid morphological classification based on thresholds on morphological parameters, in order to infer the dynamical state, could lead to contamination by other classes. Considering the dynamical classification in  $M$  distribution, the hybrid clusters in the figures, show, in fact, a not negligible superimposition over the other classes. Instead, the relaxed and disturbed distributions are enough separated, as also highlighted by the low KS-p values in Table 1, returned by the tuning procedure. To quantify what is visually represented in the figures, the median values, with 16th and 84th percentiles of the three dynamical state distributions of  $M$ , are summarised in Table 2. The superimposition between the three distributions also depends mildly on  $z$ , since in the past clusters are less relaxed than at  $z = 0$ . Looking at low and high redshift clusters, the median in Table 2 of the relaxed, hybrid and disturbed distributions are closer among each other at  $z = 1$  than at  $z = 0$ , where hybrid and disturbed medians move at higher values of  $M$ . However, the large spread of  $M$  values described by the percentiles in Table 2 do not allow any statistical significant redshift evolution of  $M$  parameter.

An even more effective way to quantify the level of contamination that might be present is to perform a ROC analysis, introduced in Sec. 4.3 and largely employed in Appendix A. In particular, in Fig. A1 we use this analysis to highlight how the morphological parameter  $M$  can effectively separate the dynamical classes defined through  $\chi$  and specifically the relaxed clusters from the disturbed (blue), from the hybrid (green), and from all non-relaxed, e.g. disturbed and hybrid (red). This was done to highlight also with ROC curves that the discrimination power of the parameter is mostly affected by the influence of the intermediate hybrid class. Considering only the disturbed cluster, the associated ROC curve is closer to the perfect case (with  $AUC \sim 0.9$  meaning that the two classes are very well separated) than if we consider only the hybrid ( $AUC \sim 0.74$ ) or taking hybrid and disturbed clusters together ( $AUC \sim 0.80$ ). Therefore the contam-



**Table 2.** Median of relaxed, hybrid and disturbed values of  $M$  distributions at  $z = 0$ ,  $z = 1$  and considering all the redshift. The first rows correspond to the  $y$  maps  $M$  parameter, while the second ones to the X-ray maps. The 16th and 84th percentiles are also listed in the table, with a  $\pm$  near the median values.

| $M$       | $z = 1$                 | $z = 0$                 | all                     |
|-----------|-------------------------|-------------------------|-------------------------|
| Relaxed   | $-0.44^{+0.49}_{-0.75}$ | $-0.49^{+0.72}_{-0.97}$ | $-0.44^{+0.60}_{-0.63}$ |
|           | $-0.48^{+0.84}_{-0.77}$ | $-0.46^{+0.71}_{-0.58}$ | $-0.47^{+0.71}_{-0.69}$ |
| Hybrid    | $-0.04^{+0.55}_{-0.48}$ | $0.35^{+0.44}_{-0.61}$  | $0.11^{+0.55}_{-0.59}$  |
|           | $-0.09^{+0.63}_{-0.58}$ | $0.30^{+0.71}_{-0.61}$  | $0.14^{+0.65}_{-0.62}$  |
| Disturbed | $0.63^{+0.49}_{-0.59}$  | $0.88^{+0.52}_{-0.63}$  | $0.76^{+0.49}_{-0.52}$  |
|           | $0.66^{+0.56}_{-0.92}$  | $0.64^{+0.81}_{-0.58}$  | $0.72^{+0.65}_{-0.66}$  |

**Table 3.** Purity and completeness, in percentage, for a selected sample of  $M$  parameter for the  $y$  maps.

| $M_y$ | Relaxed |       | Disturbed |       |
|-------|---------|-------|-----------|-------|
|       | $p$     | $C$   | $p$       | $C$   |
| -2    | 100     | 1.04  | 22.45     | 100   |
| -1.5  | 89.19   | 4.59  | 22.80     | 99.56 |
| -1    | 89.03   | 19.21 | 24.54     | 98.11 |
| -0.5  | 78.13   | 45.93 | 29.41     | 89.74 |
| 0     | 68.33   | 77.24 | 40.71     | 71.38 |
| 0.5   | 56.40   | 92.28 | 57.26     | 43.09 |
| 1     | 48.05   | 97.63 | 74.06     | 15.75 |
| 1.5   | 45.08   | 99.72 | 83.61     | 3.16  |
| 2     | 44.43   | 100   | 83.33     | 0.33  |

ination is mainly due to hybrid clusters when a threshold is chosen. From the maximum values of  $MCC$  and  $J$ , the two statistics give similar thresholds for  $M$ , all close to the expected separation value of 0:  $M_{MCC} = 0.05$  and  $M_J = 0.02$  for  $y$  maps and  $M_{MCC} = -0.03$ ,  $M_J = -0.05$  for X-ray ones.

In Tables 3 and 4, the purity  $p$  and the completeness  $C$  of the relaxed and disturbed sub-samples are shown, for a set of values of  $M$  parameter. In Fig. 7 the merit function  $P$  defined in Eq.16 (Sec. 4.3) is shown with respect to the  $M$  parameters computed in both maps and for all simulated clusters. To calculate  $P$ , we divided  $M$  values into ten equally spaced bins between their minimum and maximum values. The corresponding values of  $P$  for X-ray and  $y$  maps are shown separately in the two panels of Fig. 7. Considering that negative values of  $M$  are associated with relaxed clusters and disturbed to positive ones, it is not surprising that the trends of the relaxed and disturbed clusters are opposite and reach their maximum in the extreme values. Without the hybrid clusters, the contamination of the disturbed clusters is contained: at  $M \sim 0$  it is at the level of  $\sim 13$ -20% and lower for  $M < 0$ . Therefore, hybrid clusters represent the major source of contamination for relaxation definition, with  $P$  close to 45% at  $M \sim 0$  and  $P \sim 20\%$  at  $M \sim -1$ .

**Table 4.** Purity and completeness, in percentage, for a selected sample of  $M$  parameter for the X-ray maps.

| $M_X$ | Relaxed |       | Disturbed |       |
|-------|---------|-------|-----------|-------|
|       | $p$     | $C$   | $p$       | $C$   |
| -2    | 93.75   | 2.02  | 22.57     | 99.89 |
| -1.5  | 92.31   | 7.52  | 23.18     | 99.50 |
| -1    | 89.66   | 22.34 | 24.98     | 97.95 |
| -0.5  | 79.66   | 48.50 | 29.77     | 90.13 |
| 0     | 66.30   | 75.85 | 38.78     | 69.16 |
| 0.5   | 56.02   | 91.86 | 52.39     | 42.43 |
| 1     | 49.12   | 97.36 | 62.31     | 19.41 |
| 1.5   | 45.67   | 99.51 | 74.31     | 5.49  |
| 2     | 44.57   | 99.86 | 70.00     | 1.00  |

#### 5.4 Morphological offsets parameters results

The BCGs, estimated from  $r$  optical band maps of the clusters described in Sec. 2.2, have been identified as the most luminous galaxy inside an aperture of  $0.5R_{500}$  centred on the maximum density peak of the clusters. This is done in order to reduce the selection error of a BCG gravitationally bounded to a substructure present in the outskirts of the clusters. We recall that the pixel resolution is fixed in arcsec, one pixel in physical units span from 0.75 to 6.67 kpc moving from  $z = 0$  and  $z = 1$ . These limits are, on average, smaller than 0.05 and 0.5 per cent of  $R_{500}$ .

In Fig. 8 the distribution of the offset between the BCG position and the theoretical centre,  $\Delta_{DP-BCG}$ , is plotted. Independently of the redshift, almost 92% of the clusters in the simulation presents an offset  $\Delta_{DP-BCG} < 0.05R_{500}$  and the large majority has an offset below  $0.02R_{500}$  (see insert of the figure). The clusters with large offset are associated with objects with low values of  $\chi$  or large values of  $M$  and typically are classified as non-relaxed objects. Only 3% of relaxed clusters presents large offsets due to relaxation process still in action, highlighted by irregular morphology ( $M > 0$ ) or with a farther, slightly brighter galaxy than the one nearest the peak density.

Another result concerning the BCG position is about its variation with the redshift. Considering the median of the offset distribution, it linearly decreases by a factor of 5 from high redshift to lower redshift clusters, independently on the dynamical state as also shown in the inset in Fig. 8. The yellow area in the inset corresponds to the 16th and 84th percentile of the distributions.

We can conclude that in general the BCG position in THE THREE HUNDRED cluster sample does not depend strongly by the dynamical state and its position can be used in observations as a good tracer of the total density peak of galaxy clusters, except for a few number ( $\sim 8\%$ ) of disturbed clusters. A detailed discussion of this topic is beyond the goal of this paper, the BCG Paradigm is weakly fulfilled, since most of BCGs in THE THREE HUNDRED sample are close to the density peak, but not completely at rest. For a more detailed study of this topic, see the papers of Coziol et al. (2009); Cui et al. (2016); Harvey et al. (2017); Lopes et al. (2018); De Propriis et al. (2020).

We move now to compute the offset between the BCG centre and the ICM centres identified as ICM peaks or as ICM centroids from the X-ray and  $y$  maps (see Sec. 2.2). As before, also the offset with respect to the positions of the peaks,  $\Delta_{BCG-P_{X,y}}$ , shows no clear

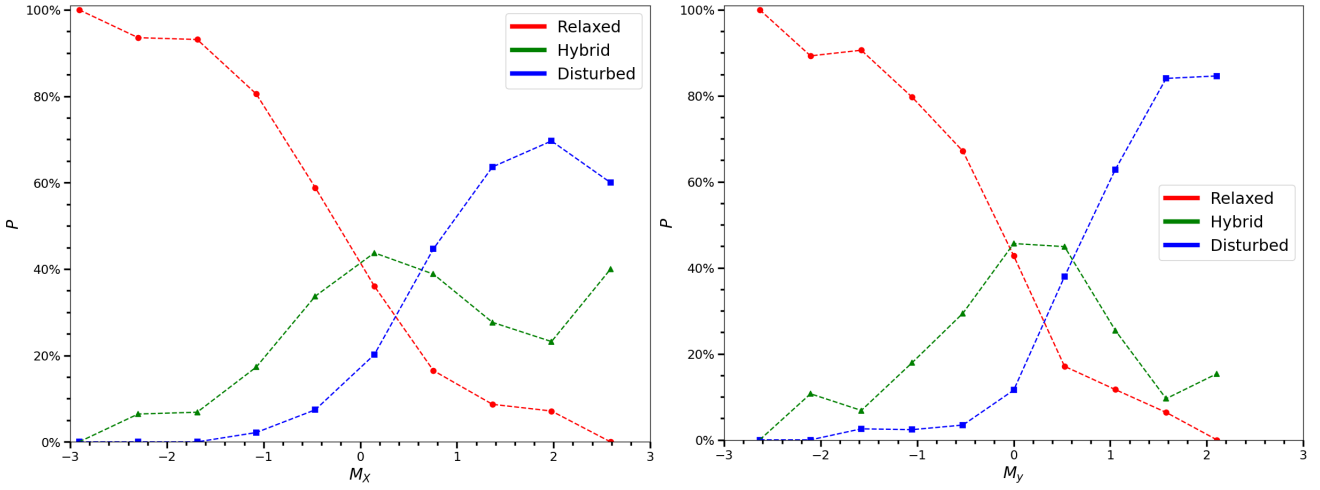


**Figure 7.** Probability functions  $P$  applied to  $M$  for X-ray data (left panel) and y maps (right panel), as defined in Eq.(16), for the  $z \in [0; 1.031]$  sample.

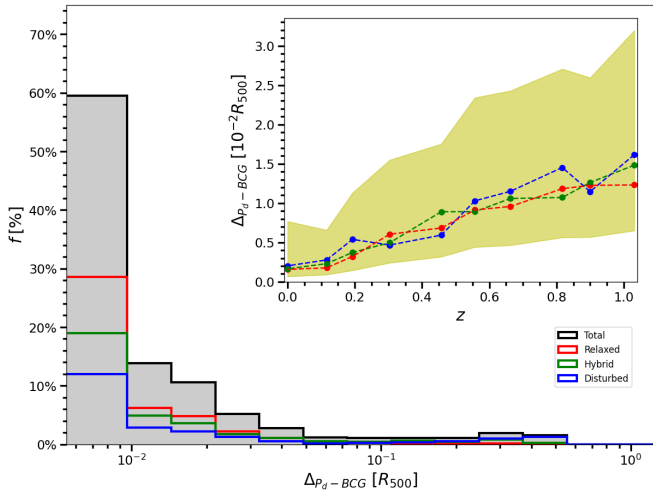


**Figure 8.** Histogram in log scale of the BCG-density peak offset,  $\Delta P_d - BCG$  and the median values of the distributions across the redshift in the inset figure.  $\Delta P_d - BCG$  is in unit of  $R_{500}$  and red, blue, green, and black lines corresponds respectively to the relaxed, disturbed, hybrid and total distributions. The left limit in the histograms correspond to the maximum resolution limit of the optical maps. The yellow area in the inset plot corresponds to the values between the 16th and 84th percentile of the distributions.

correlation with the dynamical state. Furthermore, the ROC curves present in Fig. A3 in the Appendix confirm their inefficiency: all the curves are close to the random guess line, with a redshift average AUC close to 0.63, for the binary test of the relaxed population against the non-relaxed one. In absence of strong inhomogeneities or disturbances in the ICM (like major merger events, as for cluster A370, Molnar et al. 2020), the ICM peaks are almost coincident with the total density peaks used before. Therefore both the map peaks and the BCG position are good estimates of the cluster centre.

Considering, instead, the positions of the centroids, relaxed, disturbed and hybrid clusters show different offsets with respect to all centres discussed before (the theoretical one or the total density peak, the ICM peaks and the BCG position). The centroids take into account the overall structure of the emitting ICM, resulting more affected by inhomogeneities or more in general by disturbances. The

offset between the BCG and the two centroids,  $\Delta_{BCG-C_{X,y}}$ , shows a relatively strong correlation with the dynamical state  $\chi$  indicator:  $\rho = -0.63$  for y centroid and  $\rho = -0.69$  for X-ray maps. Moreover, these offsets have also a high correlation with  $M$ :  $\rho = 0.78$  for y maps and  $\rho = 0.79$  for X-ray maps. In Fig. 9 the scatter plots and the distributions of these indicators respective to  $\chi$  and  $M$  are shown. These results are corroborated by the performance analysis of ROC curves. The centroid parameters detach from the random guess, showing  $AUC > 0.79$  if we consider the non-relaxed class and  $AUC > 0.88$  considering instead only the disturbed clusters. As expected, there are slightly better results with X-ray data, which again emphasise the presence of even small substructures: the variation with the redshift of the curves are reduced and AUC values are generally larger than y counterparts. In Fig. A2 in the Appendix, the ROC curves for the offsets parameters are shown. For completeness, the other possible offsets of the centroids with the other tracers, as the peak positions, show similar results to the BCG one. The ROC curves for centroids-peaks offsets are shown in Appendix A. For the thresholds on BCG-centroids parameters, the maximum of  $J$  and  $MCC$  are slightly different for X-ray and y data. For the offsets with X-ray centroid, the suggested threshold is on average at  $0.05 \times R_{500}$  while for y centroid it is on average at  $0.06-0.07 \times R_{500}$ .

## 5.5 Comparison with observations

As discussed in Sec. 4, a good number of papers in the literature describe the X-ray clusters properties with morphological parameters, especially for concentration and BCG offset parameters. However, a direct comparison of other results also based on different samples is not straightforward, as highlighted by Cao et al. (2020). Morphological parameters are often differently defined depending on the main topic of the paper or the limitation on the analysis procedure. Furthermore, a comparison of different clusters samples could be affected by selection effects, as the Malmquist bias, especially for flux-limited X-ray samples (Hudson et al. 2010; Chon & Böhringer 2017). In fact, Rossetti et al. (2017); Andrade-Santos et al. (2017); Chon & Böhringer (2017) have highlighted the presence of a bias between SZ and X-ray sample of cool core (CC) and non-cool core (NCC) fractions and regarding the relaxed fraction for SZ clusters ( $52 \pm 4\%$ ) sample and X-ray ( $\sim 74\%$ ) ones (Rossetti et al. 2016). In SZ clusters Lopes et al. (2018) have found a higher fraction of substructures than X-ray selected clusters. Jeltema et al. (2008) and Maughan et al.

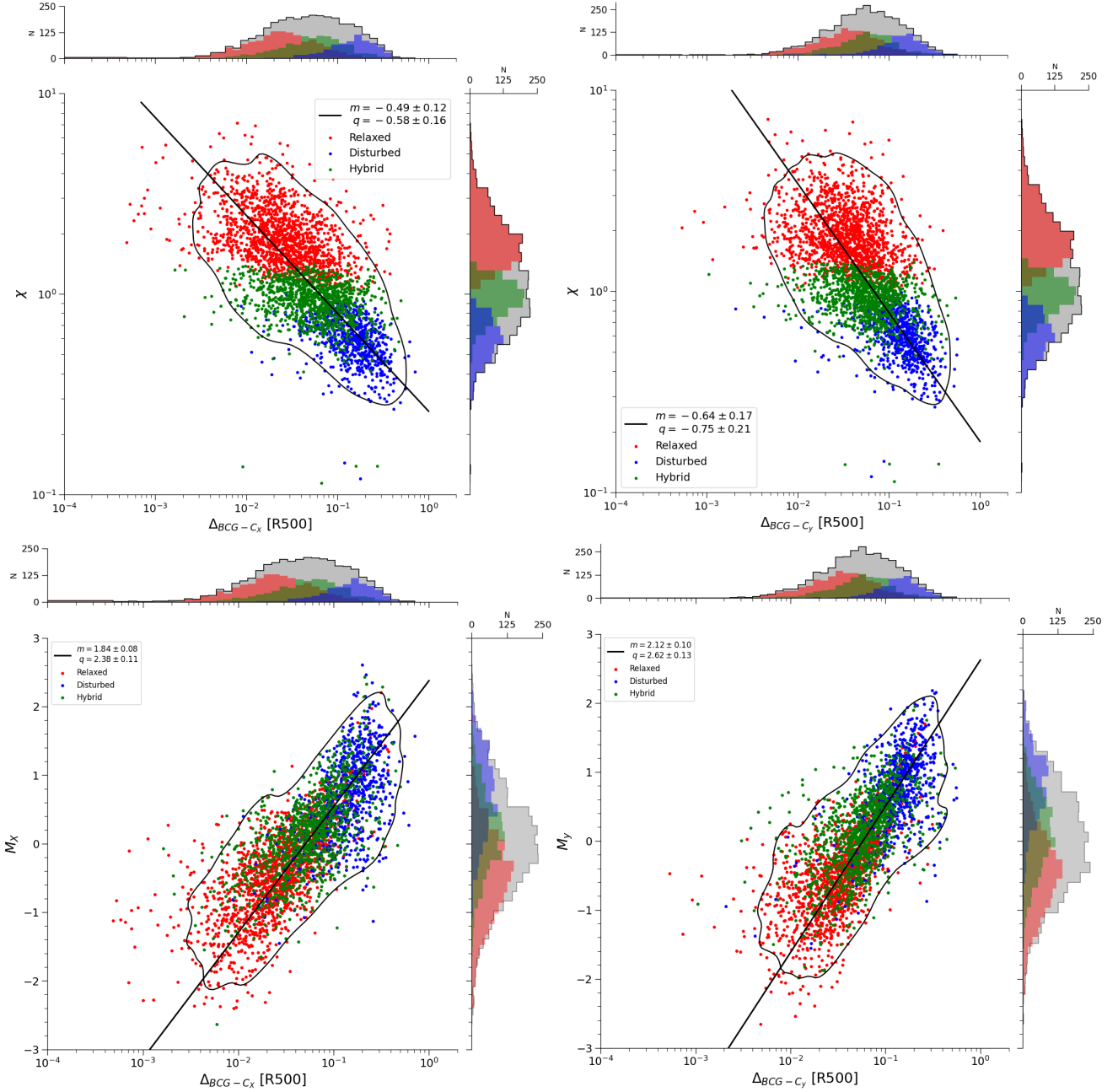


**Figure 9.** Upper panels: correlation plots in log-log scale between  $\chi$  3D parameter and the offset  $\Delta$  between BCG and X-ray (left panels) and y (right) centroids, in unit of  $R_{500}$ . Lower panels: correlation plots in log scale between  $M$  parameter calculated for X-ray and y maps and the centroid offsets. Red, green, blue colours are associated with relaxed, hybrid and disturbed clusters. The best fit and the 95% confidence level of the data distribution are also shown in the figures.

(2008) found with numerical simulations and observations a redshift evolution of the dynamical state. Instead, Bartalucci et al. (2019) found a weak evolution of their combined morphological parameter with  $z$ , while Nurgaliev et al. (2017) and McDonald et al. (2017) found no significant statistical difference using photon asymmetry,  $A_{phot}$ , and centroid shift parameters in describing X-ray morphology of X-ray and SZ selected clusters samples used, over the explored redshift range. Therefore, the number of clusters classified as relaxed vary significantly in literature according to the different samples or morphological parameters used in each paper.

The relaxed fraction that we can infer from morphological parameters in our simulated sample is close to Bartalucci et al. (2019) one

( $\sim 46\%$ ) or to SZ clusters of Rossetti et al. (2016) ( $\sim 52\%$ ) and Lopes et al. (2018) ( $49 \pm 8$ ) for the morphological indicator based on the offsets. If we apply the thresholds from  $MCC$  and  $J$  to the combined parameter  $M$ , we recover a fraction of 49-48% of relaxed clusters, while from the dynamical analysis in Sec. 5.1, the fraction of relaxed clusters for  $z \in [0, 1.031]$  is  $\sim 44\%$ . Considering instead the offset parameters between BCGs and centroids, the relaxed fractions for  $MCC$  and  $J$  thresholds are respectively 49% and 47% for  $\Delta_{BCG-C_X}$  and 57% and 47% for  $\Delta_{BCG-C_Y}$ . The large difference between  $MCC$  and  $J$  for the y offset is due to the different thresholds suggested by the two summary statistics. The peak of  $MCC$  distribution is flatter compared to  $J$ , as shown in Fig. 10, suggesting a

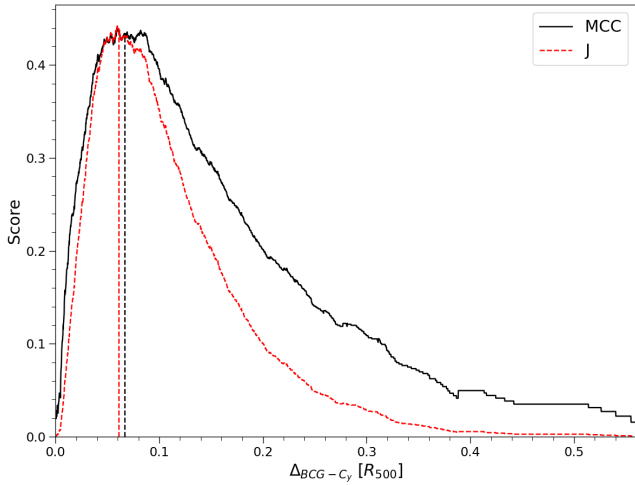


**Figure 10.** Distribution of  $MCC$  (black solid line) and  $J$  (red dashed line) for the offset parameter between BCG and  $y$  centroids, in unit of  $R_{500}$ . The inferred thresholds are represented as vertical lines in the figure

larger threshold and then, consequently, a larger fraction of relaxed clusters. The different number of relaxed clusters from dynamical to morphological parameters comes from contamination of hybrid and disturbed clusters, as explained in Sec. 5.3. The clusters that are recognised as relaxed both with dynamical indicators and  $M$  are just 32-33% of the total and the number of false detections (the non-relaxed clusters by dynamical indicators identified as relaxed by  $M$  with these thresholds) is instead close to 16%. For completeness, the number of relaxed clusters from dynamical state indicators that are not recognised as such by  $M$  is  $\sim 12\%$ . In Table B1 presents in Sec. B in the Appendix we have collected a list of the relaxed fractions available in literature, in comparison with our results. The samples differ both in redshift and mass ranges, but our results are still in agreement, considering the errors given by Rossetti et al. (2016) or Lopes et al. (2018) if we compare sub-samples with similar redshift range and medians of the previously cited work. Considering only THE THREE HUNDRED clusters with  $z \leq 0.116$ , the fraction of relaxed clusters from  $M_{X,y}$  is close to 51-54%, while for  $z \leq 0.304$  it is  $\sim 49$ -50%. For clusters in  $z \leq 0.557$  or  $z \in [0.116, 0.663]$  we have instead a 49-52% of relaxed clusters.

For a better comprehension of this topic, see the paper of Cao et al. (2020), where the consistency of relaxed fractions and the thresholding problem in the relaxation definitions are studied. However, the introduction of the combined parameter (Rasia et al. 2013; Meneghetti et al. 2014; Lovisari et al. 2017; Cialone et al. 2018; Bartalucci et al. 2019), like  $M$ , could contribute in reducing the variation in the relaxed fraction of galaxy clusters. Representing a weighted average of different clusters dynamical feature, the single definition of each used parameter lose importance in the choice of a threshold on  $M$ , avoiding non-trivial cross consistency check among different indicators. Furthermore, it gives a unique and continuous estimation of galaxy clusters regularity or relaxation, even if the performances of combined parameters must first be investigated with the advantage of numerical simulations, as was done in this paper.

## 6 CONCLUSIONS

In literature there is no consensus, both in simulations and observation (Cui et al. 2017; Cao et al. 2020), in how to divide clusters according to their dynamical state, starting from dynamical or morphological indicators. In this paper, we study the performance of these kinds of indicators using galaxy clusters from THE THREE HUNDRED Project GADGET-X simulation. From each of ten redshift snapshots between  $z \in [0; 1.031]$  that we used, we have extracted 324 galaxy clusters. From this sample, we estimated and compared the dynamical state of clusters using three different relaxation classifications. For this purpose, we used in total five 3D indicators commonly used in simulations: the total sub-halo and the most massive substructure fractions in mass  $f_s$  and  $f_{s,mm}$ , the viral ratio  $\eta$ , the centre of mass offset  $\Delta_r$  and the relaxation parameter  $\chi$ . For the same clusters, synthetic multi-wavelength images have been produced to characterise the morphological state and test the performance of the morphological indicators. In particular, we used the same six indicators, plus a combination of them, already adopted in C18, for our X-ray and  $y$  SZ parameter mock images. From the optical maps, instead, the position of the BCGs were determined to infer the dynamical state from indicators based on offsets between BCGs and X-ray or  $y$  peaks or centroids positions. Our findings can be summarised as follows:

Considering the relaxation criteria from Cui et al. (2018), C18, and a new one introduced in this work, the relaxed fractions strongly depend on which dynamical indicators are used, on the discrimination thresholds, and on the selected volume in which parameters are calculated. No remarkable difference between  $R_{200}$  and  $R_{500}$  is present for Cui et al. (2018) criterion due to the presence of  $\eta$ , while a slight increase is present with C18 one, but with a suppression of redshift evolution of the dynamical state induced by  $f_{s,mm}$ . Considering instead the dynamical classification of this work, the redshift evolution and the volume dependence are recovered for the different dynamical classes. The dynamical state, however, is better described by continuous indicators rather than classes. The introduction of  $\chi$  indicator by Hagggar et al. (2020), as a combination of dynamical indicators, has the advantage to combine the different dynamical property of the other indicators giving a single continuous indicator for the dynamical state to compare with morphological indicators.

As for the dynamical state, the morphology of galaxy clusters in X-ray and  $y$  maps is better described by the continuous combined parameter  $M$ . After the tuning procedure of the six parameters which constitute  $M$ , this parameter works efficiently and with comparable results on the two maps: for  $M_y$ - $M_X$  relation a correlation of  $\rho = 0.81$  is present and the best fit is in agreement with the identity line. Regarding the link between morphology and dynamical state,  $M$  shows a relatively strong correlation with the dynamical state parameter  $\chi$ , for which  $\rho \sim -0.66$ . Considering the dynamical classification, the major source of contamination on relaxed sub-sample is composed of hybrid clusters, as highlighted from the analysis of ROC curves. Considering two dichotomous tests between relaxed and disturbed clusters and relaxed against non-relaxed (disturbed plus hybrid) sub-samples, the ROC curves underline a decrease of performances of  $M$  discrimination ability when hybrid objects are included in the test. The area under the ROC curve decreases of  $\sim 11\%$  using the non-relaxed sample, from  $AUC \sim 0.9$  to  $\sim 0.8$ . Consequently, the rates of contamination from disturbed and hybrid clusters on relaxed sub-sample are different. From  $P$  merit function, the contamination is close to 45% for hybrid and  $\sim 20\%$  for disturbed at  $M \sim 0$ , while disturbed  $P$  decreases faster than hybrid one for negative values of  $M$ .

For the offset parameters, the position of BCGs and X-ray or



$y$  peaks are good tracers of the peak density of clusters and no remarkable differences are present in their distributions depending on the dynamical state. Therefore, the offset parameters between BCGs and X-ray,  $y$  peaks are not efficient dynamical state parameters, with ROC curves close to the performance of a random guess classifier. Considering instead the offsets between BCGs and the centroids of  $y$  or X-ray maps, the efficiency of these offset parameters are comparable to  $M$ , with  $AUC \sim 0.8$  for the binary test of relaxed with non-relaxed sub-samples. The correlation between  $M$  and these offsets are high:  $\rho = 0.78$ , while the correlation with the dynamical state is different for  $y$ :  $\rho = -0.63$  and X-ray centroids:  $\rho = -0.69$ , but both relatively strong. Similar results are obtained if peaks are used instead of BCGs positions.

Considering the lack of consensus in the literature about the actual relaxed fraction of relaxed clusters in observation, our relaxed sub-sample is comparable with Rossetti et al. (2017) and Bartalucci et al. (2019) results, and with the fraction of Lopes et al. (2018) obtained by the offset with X-ray centroids and BCGs. To be not biased by an arbitrary choice of the threshold with which segregate relaxed from non-relaxed, we use two summary statistic related to ROC curves, the Youden's  $J$  statistic and the Matthews correlation coefficient  $MCC$ . Varying the thresholds, the segregation ability of morphological indicator is maximised at the maximum values of these two variables. From their maximum, we obtain a relaxed fraction of  $\sim 48\%$  from  $M$  or the offset between BCGs and X-ray centroids, while the two thresholds on the offset with the centroids return two different fractions of relaxed clusters:  $47\%$  for  $J$  and  $57\%$  for  $MCC$ . This discrepancy is due to the relation between the dynamical state and the offsets parameters. A difference of  $1\%$  in the offset corresponds to a variation of  $10\%$  in the relaxed fraction, underling how problematic the thresholding problem could be for relaxation definition.

## ACKNOWLEDGEMENTS

This work has been made possible by THE THREE HUNDRED Collaboration. The simulations used in this paper have been performed in the MareNostrum Supercomputer at the Barcelona Supercomputing Center, thanks to CPU time granted by the Red Española de Supercomputación. As part of THE THREE HUNDRED Project, this work has received financial support from the European Union's Horizon 2020 Research and Innovation programme under the Marie Skłodowska-Curie grant agreement number 734374, the LACEGAL project.

MDP and FDL acknowledge support from Sapienza Università di Roma thanks to Progetti di Ricerca Medi 2019, prot. RM11916B7540DD8D. WC acknowledges support from the European Research Council under grant number 670193 (the COSFORM project). GY and AK acknowledge financial support from *Ministerio de Ciencia, Innovación y Universidades / Fondo Europeo de Desarrollo Regional* (Spain), under research grant PGC2018-094975-C21.

## DATA AVAILABILITY

The data used in this paper is part of THE THREE HUNDRED Project and can be accessed following the guide lines of the collaboration that can be found in the main website<sup>5</sup> of the collaboration. The data specifically shown in this paper will be shared upon request to the authors.

## REFERENCES

- Andrade-Santos F., et al., 2017, *ApJ*, 843, 76  
 Ansarifard S., et al., 2020, *A&A*, 634, A113  
 Arthur J., et al., 2019, *MNRAS*, 484, 3968  
 Baldi A. S., De Petris M., Sembolini F., Yepes G., Cui W., Lamagna L., 2018, *MNRAS*, 479, 4028  
 Barnes D. J., et al., 2017, *MNRAS*, 471, 1088  
 Bartalucci I., Arnaud M., Pratt G. W., Démoclès, J. Lovisari L., 2019, *A&A*, 628, A86  
 Biffi V., et al., 2016, *ApJ*, 827, 112  
 Birkinshaw M., 1999, *Phys. Rep.*, 310, 97  
 Böhringer H., et al., 2010, *A&A*, 514, A32  
 Buote D. A., Tsai J. C., 1995, *ApJ*, 452, 522  
 Cao K., Barnes D. J., Vogelsberger M., 2020, arXiv e-prints, p. [arXiv:2006.10752](https://arxiv.org/abs/2006.10752)  
 Capalbo V., De Petris M., De Luca F., Cui W., Yepes G., Knebe A., Rasia E., 2020, arXiv e-prints, p. [arXiv:2009.04565](https://arxiv.org/abs/2009.04565)  
 Carlstrom J. E., Holder G. P., Reese E. D., 2002, *ARA&A*, 40, 643  
 Cassano R., Ettori S., Giacintucci S., Brunetti G., Markevitch M., Venturi T., Gitti M., 2010, *ApJ*, 721, L82  
 Chabrier G., 2003, *PASP*, 115, 763  
 Chon G., Böhringer H., 2017, *A&A*, 606, L4  
 Cialone G., De Petris M., Sembolini F., Yepes G., Baldi A. S., Rasia E., 2018, *MNRAS*, 477, 139  
 Coziol R., Andernach H., Caretta C. A., Alamo-Martínez K. A., Tago E., 2009, *AJ*, 137, 4795  
 Cui W., Springel V., Yang X., De Lucia G., Borgani S., 2011, *MNRAS*, 416, 2997  
 Cui W., et al., 2014, *MNRAS*, 437, 816  
 Cui W., et al., 2016, *MNRAS*, 456, 2566  
 Cui W., Power C., Borgani S., Knebe A., Lewis G. F., Murante G., Poole G. B., 2017, *MNRAS*, 464, 2502  
 Cui W., et al., 2018, *MNRAS*, 480, 2898  
 De Propriis R., et al., 2020, *MNRAS*  
 Duffy A. R., Schaye J., Kay S. T., Dalla Vecchia C., 2008, *MNRAS: Letters*, 390, L64  
 Fawcett T., 2006, *Pattern Recognition Letters*, 27, 861  
 Ge C., Wang Q. D., Burchett J. N., Tripp T. M., Sun M., Li Z., Gu Q., Ji L., 2018, *MNRAS*, 481, 4111  
 Gianfagna G., et al., 2020, arXiv e-prints, p. [arXiv:2010.03634](https://arxiv.org/abs/2010.03634)  
 Haggard R., Gray M. E., Pearce F. R., Knebe A., Cui W., Mostoghiu R., Yepes G., 2020, *MNRAS*, 492, 6074  
 Harvey D., Courbin F., Kneib J. P., McCarthy I. G., 2017, *MNRAS*, 472, 1972  
 Henson M. A., Barnes D. J., Kay S. T., McCarthy I. G., Schaye J., 2016, *MNRAS*, 465, 3361  
 Hudson D. S., Mittal R., Reiprich T. H., Nulsen P. E. J., Andernach H., Sarazin C. L., 2010, *A&A*, 513, A37  
 Infantino M., et al., 2020, *Journal of Medical Virology*, 92, 1671  
 Jeltema T. E., Hallman E. J., Burns J. O., Motl P. M., 2008, *ApJ*, 681, 167  
 Klypin A. A., Trujillo-Gomez S., Primack J., 2011, *ApJ*, 740, 102  
 Klypin A., Yepes G., Gottlöber S., Prada F., Heß S., 2016, *MNRAS*, 457, 4340  
 Knebe A., et al., 2020, *MNRAS*, 495, 3002  
 Knollmann S. R., Knebe A., 2009, *ApJS*, 182, 608  
 Kuchner U., et al., 2020, *MNRAS*, 494, 5473  
 Lavoie S., et al., 2016, *MNRAS*, 462, 4141  
 Li Q., et al., 2020, *MNRAS*, 495, 2930  
 Lin Y.-T., Mohr J. J., 2004, *ApJ*, 617, 879  
 Lopes P. A. A., Trevisan M., Laganá T. F., Durret F., Ribeiro A. L. B., Rembold S. B., 2018, *MNRAS*, 478, 5473  
 Lotz J. M., Primack J., Madau P., 2004, *AJ*, 128, 163  
 Lovisari L., et al., 2017, *ApJ*, 846, 51  
 Macciò A. V., Dutton A. A., Van Den Bosch F. C., Moore B., Potter D., Stadel J., 2007, *MNRAS*, 378, 55  
 Macciò A. V., Dutton A. A., Van Den Bosch F. C., 2008, *MNRAS*, 391, 1940  
 Mahdavi A., Hoekstra H., Babul A., Bildfell C., Jeltema T., Henry J. P., 2013,

<sup>5</sup> <https://the300-project.org>

- ApJ*, 767, 116
- Mann A. W., Ebeling H., 2012, *MNRAS*, 420, 2120
- Mantz A. B., Allen S. W., Morris R. G., Schmidt R. W., von der Linden A., Urban O., 2015, *MNRAS*, 449, 199
- Maughan B. J., Jones C., Forman W., Speybroeck L. V., 2008, *ApJS*, 174, 117
- Maughan B. J., Giles P. A., Randall S. W., Jones C., Forman W. R., 2012, *MNRAS*, 421, 1583
- McDonald M., et al., 2017, *ApJ*, 843, 28
- Meneghetti M., et al., 2014, *ApJ*, 797, 34
- Mohr J. J., Fabricant D. G., Geller M. J., 1993, *ApJ*, 413, 492
- Molnar S. M., Ueda S., Umetsu K., 2020, *ApJ*, 900, 151
- Mostoghiu R., Knebe A., Cui W., Pearce F. R., Yepes G., Power C., Dave R., Arth A., 2019, *MNRAS*, 483, 3390
- Muldrew S. I., Hatch N. A., Cooke E. A., 2015, *MNRAS*, 452, 2528
- Nagai D., Kravtsov A. V., Vikhlinin A., 2007, *ApJ*, 668, 1
- Nelson K., Lau E. T., Nagai D., Rudd D. H., Yu L., 2014, *ApJ*, 782, 107
- Neto A. F., et al., 2007, *MNRAS*, 381, 1450
- Nurgaliev D., McDonald M., Benson B. A., Miller E. D., Stubbs C. W., Vikhlinin A., 2013, *ApJ*, 779, 112
- Nurgaliev D., et al., 2017, *ApJ*, 841, 5
- O'Hara T. B., Mohr J. J., Bialek J. J., Evrard A. E., 2006, *ApJ*, 639, 64
- Okabe N., Zhang Y.-Y., Finoguenov A., Takada M., Smith G. P., Umetsu K., Futamase T., 2010, *ApJ*, 721, 875
- Parekh V., van der Heyden, K. Ferrari, C. Angus, G. Holwerda, B. 2015, *A&A*, 575, A127
- Pearce F. A., Kay S. T., Barnes D. J., Bower R. G., Schaller M., 2020, *MNRAS*, 491, 1622
- Pinkney J., Roettiger K., Burns J. O., Bird C. M., 1996, *ApJS*, 104, 1
- Planck Collaboration et al., 2016, *A&A*, 594, A13
- Planelles S., et al., 2017, *MNRAS*, 467, 3827
- Poole G. B., Fardal M. A., Babul A., McCarthy I. G., Quinn T., Wadsley J., 2006, *MNRAS*, 373, 881
- Postman M., Lauer T. R., 1995, *ApJ*, 440, 28
- Pratt G. W., Arnaud M., Biviano A., Eckert D., Ettori S., Nagai D., Okabe N., Reiprich T. H., 2019, *Space Sci. Rev.*, 215, 25
- Rasia E., et al., 2012, *New Journal of Physics*, 14, 055018
- Rasia E., Meneghetti M., Ettori S., 2013, *Astronomical Review*, 8, 40
- Rasia E., et al., 2014, *ApJ*, 791, 96
- Rau A., et al., 2013, arXiv e-prints, p. arXiv:1308.6785
- Rossetti M., et al., 2016, *MNRAS*, 457, 4515
- Rossetti M., Gastaldello F., Eckert D., Della Torre M., Pantiri G., Cazzoletti P., Molendi S., 2017, *MNRAS*, 468, 1917
- Sanderson A. J. R., Edge A. C., Smith G. P., 2009, *MNRAS*, 398, 1698
- Santos J. S., Rosati P., Tozzi P., Böhringer H., Ettori S., Bignamini A., 2008, *A&A*, 483, 35
- Schade D., Lilly S. J., Crampton D., Hammer F., Fèvre O. L., Tresse L., 1995, *ApJ*, 451
- Sembolini F., Yepes G., De Petris M., Gottlöber S., Lamagna L., Comis B., 2012, *MNRAS*, 429, 323
- Sunyaev R. A., Zeldovich Y. B., 1972, Comments on Astrophysics and Space Physics, 4, 173
- Sunyaev R. A., Zeldovich I. B., 1980, *ARA&A*, 18, 537
- Swets J. A., 1988, *Science*, 240, 1285
- Tremaine S., 1990, The origin of central cluster galaxies.. Wielen, Roland (Ed.), pp 394–405
- Voit G. M., 2005, *Rev. Mod. Phys.*, 77, 207
- Wang Y., et al., 2018, *ApJ*, 868, 130
- Yuan Z. S., Han J. L., 2020, *MNRAS*, 497, 5485
- Zenteno A., et al., 2020, *MNRAS*
- Zhang Y.-Y., et al., 2010, *ApJ*, 711, 1033
- ZuHone J. A., Biffi V., Hallman E. J., Randall S. W., Foster A. R., Schmid C., 2014, arXiv e-prints, p. arXiv:1407.1783

## APPENDIX A: ROC ANALYSIS ON MORPHOLOGICAL PARAMETERS

ROC curves, initially introduced as a method to characterise radar receivers, are now largely used in many scientific applications, as medicine (Infantino et al. 2020) or machine learning techniques for dichotomous (or more) classifiers. The main advantage of ROC analysis is that represents graphically the diagnostic ability of a test when an arbitrary threshold is varied.

In our work, we decided to use ROC curves to illustrate the thresholding problem of relaxed definition of galaxy clusters. As outlined in Sec. 5.5, or more completely by Cao et al. (2020), there is no consensus in the literature on which threshold to use for a given morphological parameter. This leads to different relaxation criteria that could be very restrictive or not. A ROC inspection of the diagnostic power could give a criterion to select which are the best parameters to use in observation and give information about possible threshold on them, binding their definition to some summary statistic drawn from the curve, as it was done here with *AUC*, *MCC*, and *J*.

In Fig. A1 and Fig. A2, the ROC curves for morphological parameters *M* and the offset between the BCG and the two centroids ( $\Delta_{BCG-C_{X,Y}}$ ) for X-ray and y maps are shown. The two morphological parameters are more efficient in separating the two extremes of the dynamical state: the disturbed ROC curves are always higher than hybrid ones, as the area under the curve: *AUC*  $\sim$  0.90 for disturbed and *AUC*  $\sim$  0.74 when we consider only the hybrid in the test. As a result, if we are interested to extract a relaxed sub-sample, the possible contaminants consist mainly of hybrid clusters. Comparing the relaxed and non-relaxed objects we have an intermediate performance, with *AUC*  $\sim$  0.80.

In Fig. A3, we show the difference of performances when the peaks are used instead of centroids. Comparing the curves in Fig. A2 and A3, a sharp drop in performance is evident when the peak is used: *AUC* falls by  $\sim$  0.20 and the ROC curves are closed to the identity line, that in this plane represents the performance of a random guess classifier. This lack of performances is related to X-ray or y peaks positions, that are not good indicators of the dynamical state but are reliable tracers of the peak density of galaxy clusters. All the possible offsets between BCG, X-ray or y peaks, and peak density show no dependence from the dynamical state and have similar ROC curves of the ones present in Fig. A3. As a result, using the positions of the peaks or BCGs do not affect dramatically the results, as shown in Fig. A4, where the offsets  $\Delta_{P_y-C_y}$  between the X-ray or y centroids and their peak are shown. The *AUC* for centroids-peaks offsets are slightly lower than BCG ones: *AUC*  $\sim$  0.88-0.89 for disturbed and *AUC*  $\sim$  0.76-0.79 for non-relaxed classes.

## APPENDIX B: LITERATURE RELAXED FRACTION

In Table B1, we list a collection of relaxed fractions of galaxy clusters in literature, in comparison with our findings. For the THREE HUNDRED sample, we have excluded the relaxed fraction of clusters from y centroid-BCG positions offset parameter with the *MCC* threshold, that it is instead of 57% of the total number of clusters. Considering the cool-core clusters as relaxed clusters, in the table we listed as relaxed the cool-core fractions of clusters obtained from thresholds on concentration ratio parameter *c*. However, these fractions are affected by the cool-core bias between SZ and X-ray selected sample, as described in the works of Rossetti et al. (2017); Andrade-Santos et al. (2017); Chon & Böhringer (2017). For some of the listed works, the authors do not specify the relaxed fraction from the used morphological indicators. The relaxed fractions in Table B1 are calculated

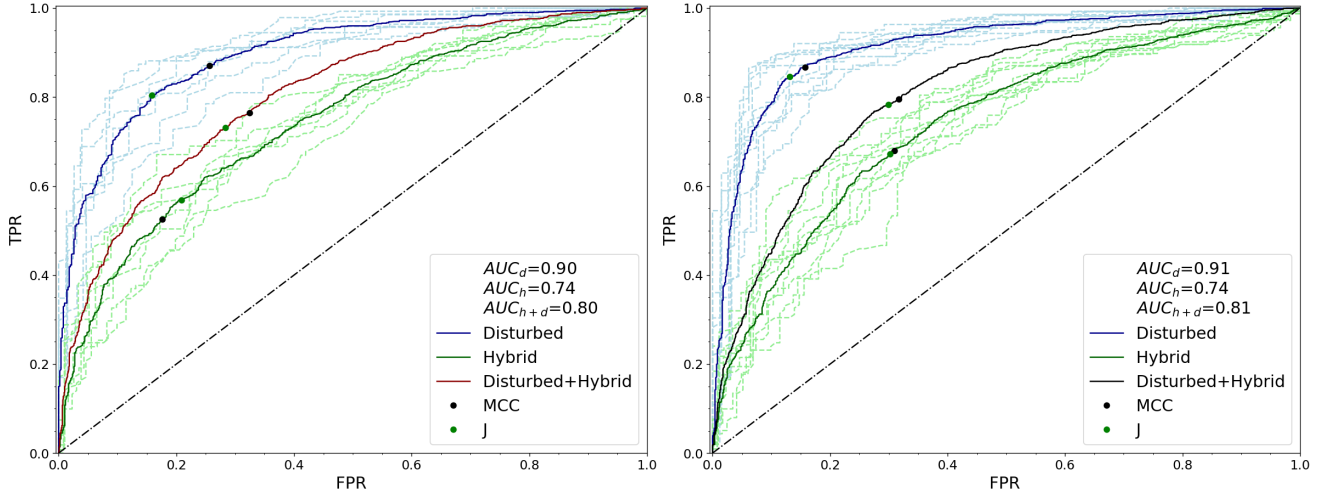


**Figure A1.** ROC curves for X-ray (left panel) and  $y$  (right panel)  $M$  parameter. Blue and green lines correspond respectively to the binary test of relaxed against only disturbed or hybrid clusters. The coloured dashed lines are the ROC curves of  $M$  estimated in each redshift bin. The curves of the complete redshift sample ( $z \in [0, 1.031]$ ) are drawn as solid lines. The dichotomous test of relaxed versus the non-relaxed (disturbed plus hybrid) sub-samples is shown as a solid black line. The green and black points correspond to the  $(TPR; FPR)$  values of  $MCC$  and  $J$  inferred thresholds. The identity line corresponds to a random guess classifier.

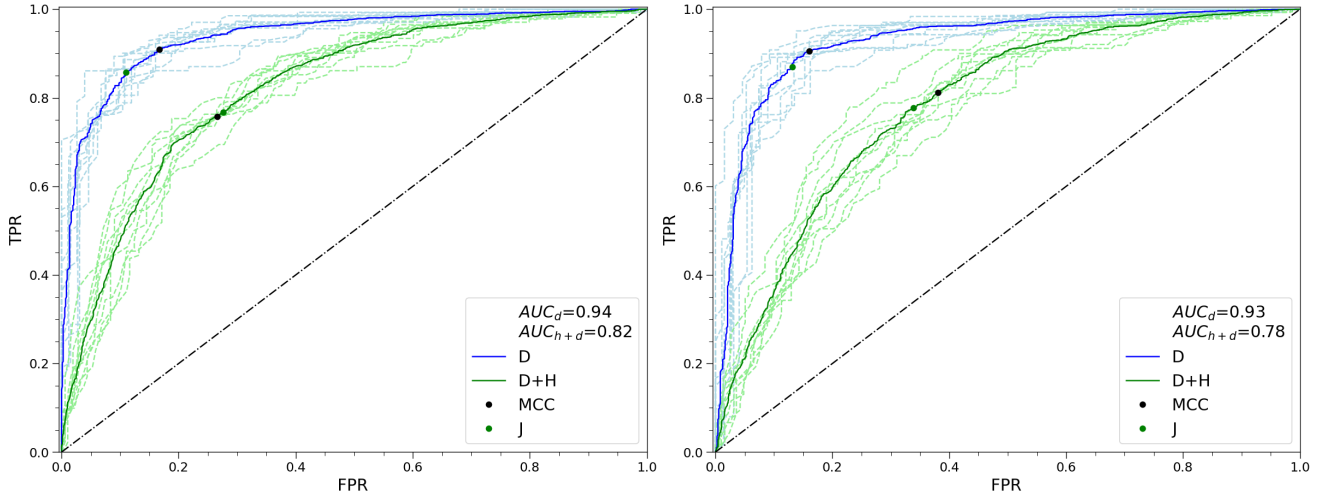


**Figure A2.** ROC curves for X-ray (left panel) and  $y$  (right) centroids offset parameters. Blue and green lines correspond respectively to the binary test of relaxed against only disturbed and disturbed plus hybrid classes. Dashed lines are associated with each single redshift curve and solid ones considering the complete redshift sample. The  $TPR$  and  $FPR$  values of  $MCC$  and  $J$  thresholds are also shown as green and black points in the figures.

according to their criteria, considering the data present in their table or figures. These values are marked in the table with a (\*), near the reference. We further note that this unbiased selection simply includes all the works with different observations, methods, criteria and thresholds. No normalisation nor correction is included.

This paper has been typeset from a  $\text{\LaTeX}$  file prepared by the author.

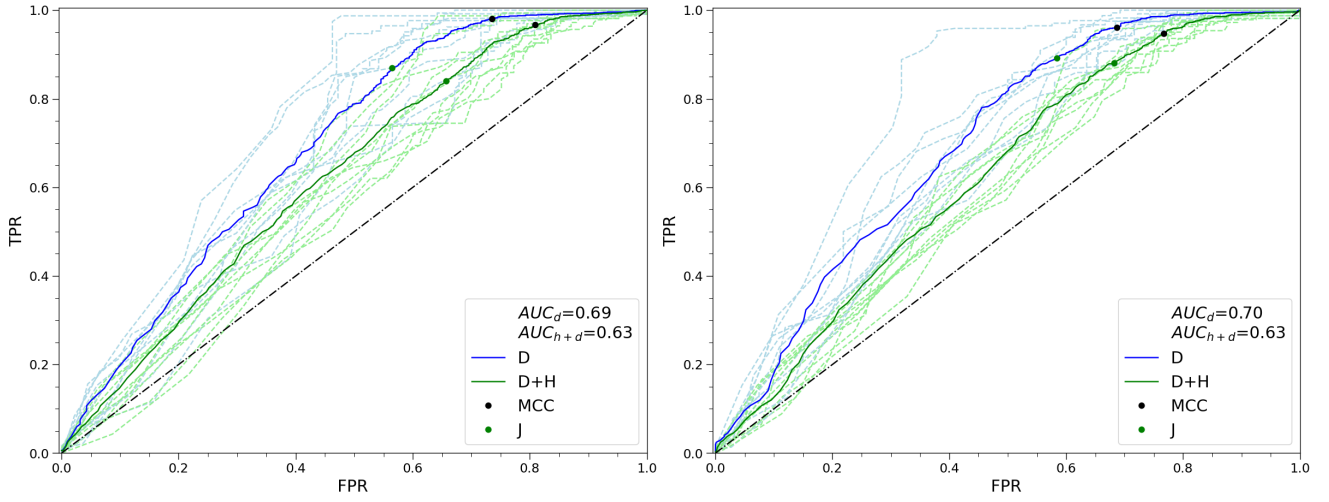


**Figure A3.** As in Fig. A2, but using the offset parameter between BCGs and X-ray (left panel) and y (right) peaks.

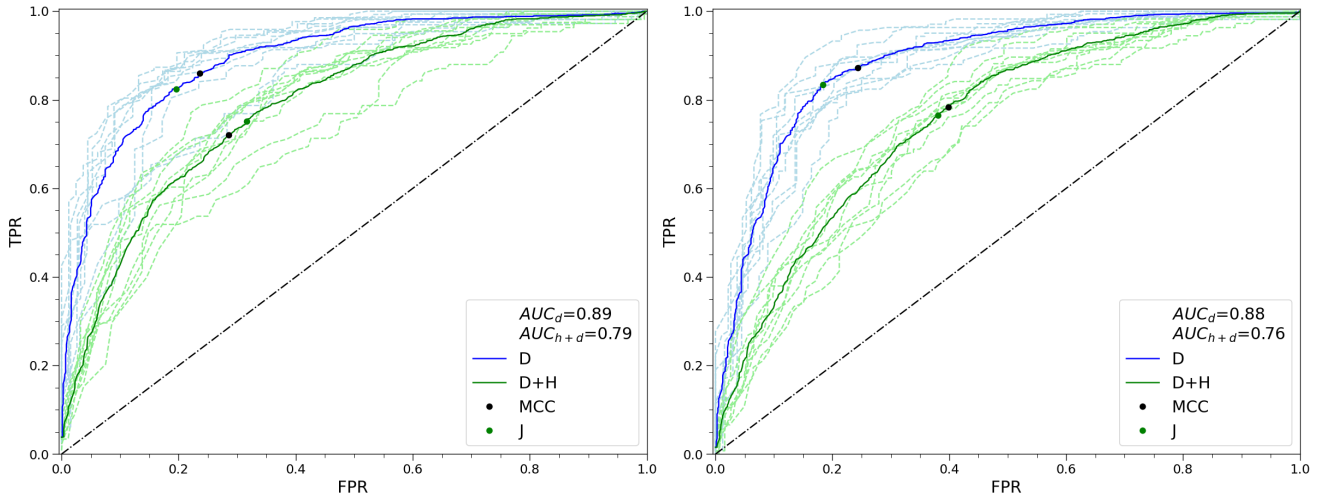


**Figure A4.** As in Fig. A2, considering the X-ray (left panel) and y (right) centroids-peaks offset parameters.



**Table B1.** Relaxed fractions in literature samples compared with THE THREE HUNDRED one. The samples properties are summarised considering the number of objects and the redshift ranges of the clusters. The (\*) symbol denotes the works for which the relaxed fractions are deduced from the tables or figures present in the papers.

| Paper  | Number of objects | Relaxed fractions [%] | redshift  |           |
|--|-------------------|-----------------------|-----------|-----------|
|  |                   |                       | $z_{min}$ | $z_{max}$ |
| THE THREE HUNDRED                                      | 3240              | 47-49                 | -         | < 1.031   |
| Santos et al. (2008) (low z)                           | 11                | 64                    | 0.15      | 0.3       |
| Santos et al. (2008) (high z)                          | 15                | 73                    | 0.7       | 1.39      |
| Sanderson et al. (2009)                                | 65                | 37                    | 0.15      | 0.3       |
| Zhang et al. (2010)*<br>or Okabe et al. (2010)*        | 12                | 42                    | 0.15      | 0.3       |
| Cassano et al. (2010)*                                 | 32                | 44                    | 0.2       | 0.4       |
| Böhringer et al. (2010)*                               | 31                | 48                    | 0.06      | 0.18      |
| Mann & Ebeling (2012)*                                 | 108               | 44                    | 0.15      | 0.7       |
| Maughan et al. (2012)*                                 | 114               | 18 – 25               | 0.1       | 1.3       |
| Mahdavi et al. (2013)*                                 | 50                | 26 – 28               | 0.15      | 0.55      |
| Nurgaliev et al. (2013)                                | 36                | 33                    | 0.3       | 0.9       |
| Parekh et al. (2015)                                   | 84                | 23                    | 0.02      | 0.9       |
| Mantz et al. (2015)                                    | 361               | 16                    | 0.05      | 1.2       |
| Lavoie et al. (2016)                                   | 85                | 65                    | 0.043     | 1.05      |
| Rossetti et al. (2016) (SZ sample)                     | 132               | 52 ± 4                | 0.02      | 0.87      |
| Rossetti et al. (2017) (SZ sample)                     | 169               | 29 ± 4                | 0.04      | 0.87      |
| Rossetti et al. (2017) (X-ray)                         | 104               | 59 ± 5                | 0.15      | 0.7       |
| Andrade-Santos et al. (2017) (SZ sample)               | 164               | 28-39                 | -         | < 0.35    |
| Andrade-Santos et al. (2017) (X-ray)                   | 100               | 44-64                 | 0.025     | 0.3       |
| Lovisari et al. (2017)*                                | 120               | 32                    | 0.01      | 0.55      |
| Chon & Böhringer (2017) (Volume limited sample)        | 93                | 29                    | -         | < 0.1     |
| Chon & Böhringer (2017) (Flux limited sample 1)        | 51                | 41                    | -         | < 0.1     |
| Chon & Böhringer (2017) (Flux limited sample 2)        | 42                | 43                    | -         | < 0.1     |
| Lopes et al. (2018) (X-ray sample, optical indicators) | 62                | 47-66                 | 0.01      | 0.1       |
| Lopes et al. (2018) (X-ray sample, X-ray indicators)   | 62                | 65-69                 | 0.01      | 0.1       |
| Lopes et al. (2018) (SZ sample, optical indicators)    | 40                | 38-63                 | 0.01      | 0.1       |
| Lopes et al. (2018) (SZ sample, X-ray indicators)      | 40                | 48-53                 | 0.01      | 0.1       |
| Bartalucci et al. (2019)*                              | 74                | 46                    | 0.08      | 1.13      |
| Zenteno et al. (2020)                                  | 288               | 14                    | 0.1       | 0.9       |
| Yuan & Han (2020)                                      | 964               | 51.2                  | 0.003     | 1.75      |